

1 **Main Manuscript for**

2 **Unexpected anthropogenic emission decreases explain recent atmospheric**
3 **mercury concentration declines**

4
5 Aryeh Feinberg^{a*}, Noelle E. Selin^{a,b}, Christine F. Braban^c, Kai-Lan Chang^{d,e}, Danilo Custódio^f, Daniel A.
6 Jaffe^{g,h}, Katriina Kyllönenⁱ, Matthew S. Landis^j, Sarah R. Leeson^c, Winston Luke^k, Koketso M. Molepo^l,
7 Marijana Murovec^m, Michelle G. Nerentorp Mastromonacoⁿ, Katrine Aspomo Pfaffhuber^o, Julian Rüdiger^p,
8 Guey-Rong Sheu^q, and Vincent L. St.Louis^r

9 ^a *Institute for Data, Systems, and Society, Massachusetts Institute of Technology, Cambridge, MA 02139,*
10 *USA*

11 ^b *Department of Earth, Atmospheric, and Planetary Sciences, Massachusetts Institute of Technology,*
12 *Cambridge, MA 02139, USA*

13 ^c *UK Centre for Ecology & Hydrology (UKCEH), Penicuik, Midlothian EH26 0QB, UK*

14 ^d *Cooperative Institute for Research in Environmental Sciences, University of Colorado, Boulder, CO*
15 *80309-0401, USA*

16 ^e *NOAA Chemical Sciences Laboratory, Boulder, CO 80305, USA*

17 ^f *Max-Planck-Institut für Biogeochemie, D-07745 Jena, Germany*

18 ^g *School of STEM, University of Washington Bothell, Bothell, WA 98011, USA*

19 ^h *Department of Atmospheric Sciences, University of Washington Seattle, Seattle, WA 98195, USA*

20 ⁱ *Finnish Meteorological Institute, Helsinki 00560, Finland*

21 ^j *United States Environmental Protection Agency, Office of Research and Development, Research*
22 *Triangle Park, NC 27711, USA*

23 ^k *NOAA/Air Resources Laboratory, College Park, MD 20740, USA*

24 ^l *Institute of Coastal Environmental Chemistry, Helmholtz Zentrum Hereon, 21502 Geesthacht, Germany*

25 ^m *Slovenian Environment Agency, Environment and Nature protection Office, Air Quality Division, 1000*
26 *Ljubljana, Slovenia*

27 ⁿ *IVL Swedish Environmental Research Institute, SE-411 33 Gothenburg, Sweden*

28 ^o *NILU, 2027 Kjeller, Norway*

29 ^p *Air Monitoring Network, German Environment Agency, 63225 Langen, Germany*

30 ^q *Department of Atmospheric Sciences, National Central University, Taoyuan 320, Taiwan*

31 ^r *Department of Biological Sciences, University of Alberta, Edmonton, AB T6G 2E9, Canada*

32

33 *Correspondence to: arifeinberg@gmail.com (A.F.)

34

35

36 **Author Contributions:** A.F. and N.E.S. designed the research. K.-L.C. advised the implementation of
37 statistical methods. C.F.B., D.C., D.A.J., K.K., M.S.L., S.R.L., W.L., K.M.M., M.M., M.G.N.M., K.A.P., J.R.,
38 G.-R.S., and V.L.S.L. contributed Hg observation data. A.F. performed the analysis and wrote the
39 manuscript under the supervision of N.E.S., with inputs and discussion from all authors. Author order is
40 alphabetical following the second author, N.E.S.

41

42 **Competing Interest Statement:** The authors declare no competing interests.

43

44 **Classification:** Physical Sciences/Earth, Atmospheric, and Planetary Sciences

45

46 **Keywords:** mercury trends; anthropogenic emissions; atmospheric observations; Minamata Convention
47 on Mercury; biogeochemical box model; chemistry-transport model.

48

49 **This PDF file includes:**

50 Main Text

51 Figures 1 to 4

52 Table 1

53

54 **Abstract**

55 Anthropogenic activities emit $\sim 2000 \text{ Mg yr}^{-1}$ of the toxic pollutant mercury (Hg) into the atmosphere,
56 leading to long-range transport and deposition to remote ecosystems. Global anthropogenic emissions
57 inventories report increases in Northern Hemispheric (NH) Hg emissions during the last three decades, in
58 contradiction with the observed decline in atmospheric Hg concentrations at NH measurement stations.
59 Many factors can obscure the link between anthropogenic emissions and atmospheric Hg concentrations,
60 including trends in the re-emissions of previously released anthropogenic (“legacy”) Hg, atmospheric sink
61 variability, and spatial heterogeneity of monitoring data. Here we assess the observed trends in gaseous
62 elemental mercury (Hg^0) in the NH and apply biogeochemical box modeling and chemical transport
63 modeling to understand the trend drivers. Using linear mixed effects modeling of observational data from
64 51 stations, we find negative Hg^0 trends in most NH regions, with an overall trend for 2005–2020 of
65 $-0.011 \pm 0.006 \text{ ng m}^{-3} \text{ yr}^{-1}$ ($\pm 2 \text{ SD}$). In contrast to existing emission inventories, our modelling analysis
66 suggests that NH anthropogenic emissions must have declined by at least 140 Mg yr^{-1} between the years
67 2005 and 2020 to be consistent with observed trends. Faster declines in 95th percentile Hg^0 values than
68 median values in Europe, North America, and East Asian measurement stations corroborate that the
69 likely cause is a decline in nearby anthropogenic emissions rather than background legacy re-emissions.
70 Our results are relevant for evaluating the effectiveness of the Minamata Convention on Mercury,
71 demonstrating that existing emissions inventories are incompatible with the observed Hg^0 declines.

72

73 **Significance statement**

74 Mercury (Hg) is a global pollutant that bioaccumulates to toxic concentrations along the food chain.
75 Anthropogenic Hg inventories suggest increasing global emissions over recent decades, which is at odds
76 with observed declines of atmospheric Hg concentrations in the Northern Hemisphere (NH). We use
77 statistical and process-based modeling to rule out the possibility that NH anthropogenic emissions of Hg
78 could have increased while atmospheric Hg concentrations declined. This implies that anthropogenic
79 emissions of Hg have very likely declined in recent years. This work informs the effectiveness evaluation
80 of the international Minamata Convention on Mercury. Further research is required to better link emission
81 changes with measured concentrations so that the specific causes of global Hg trends can be identified.

82

83 **Main Text**

84

85 **Introduction**

86 The global Minamata Convention on Mercury is a multilateral environmental agreement that aims to
87 “protect human health and the environment from anthropogenic emissions and releases of mercury”, a
88 neurotoxic pollutant (1). As mercury (Hg) is volatile and long-lived (~ 6 months) in the atmosphere (2),
89 trends in atmospheric mercury concentrations are one of the proposed indicators that will be used to
90 evaluate the Convention’s effectiveness (3). However, linking trends in Hg concentrations and
91 anthropogenic emissions is not a straightforward process. The major anthropogenic emissions sources of
92 Hg, including artisanal and small-scale gold mining (ASGM), coal combustion, and industrial processes,
93 are distributed heterogeneously across the globe (4, 5). At the same time, legacy re-emissions of
94 historical anthropogenic mercury from soils, freshwater, wildfires, and oceans are diffuse background
95 sources, which are thought to make up a larger fraction of the overall Hg source fluxes (60% for legacy
96 re-emissions vs. 27% for primary anthropogenic) (6). Atmospheric Hg monitoring stations are also not
97 evenly distributed globally, with more stations located in North America and Europe (7), and they cover
98 different time periods. Therefore, statistical modeling is necessary to maximize the information present in
99 atmospheric Hg records (8), while mechanistic modeling helps connect observed Hg concentrations with
100 their drivers, i.e., emissions, chemical transformations, transport, and deposition (7).

101

102 The large-scale trends of atmospheric Hg over the last three decades have been under recent debate.
103 Bottom-up inventories show increasing global anthropogenic emissions since the 1990s (5, 9, 10), which,
104 all else being equal, should increase atmospheric Hg concentrations. However, in North America and
105 Europe, measured gaseous elemental mercury (GEM: Hg⁰) concentrations have generally been declining
106 since continuous measurements began in the 1990s (7, 11–14). There is a clear need to understand this
107 contradiction and evaluate past trends of Hg emissions, especially after the adoption of the Minamata
108 Convention in 2013. Zhang et al. (7), the most recent study to evaluate the consistency between emission
109 inventories and atmospheric observations using the chemical-transport model GEOS-Chem, analyzed
110 available data through 2014. Their comparison between the model and measurements from North
111 America and Europe led the authors to conclude that anthropogenic Hg emissions declined by ~30%
112 between 1990 and 2010, due to weaker increases of Hg emissions from ASGM and strong declines in Hg
113 emissions from commercial products (7). More recent measurements from East Asian stations have also
114 reported declines in atmospheric Hg (15–18). Long term measurements from the Southern Hemisphere
115 (SH) remain scarce, with the latest results from the observation stations Cape Point and Amsterdam
116 Island showing insignificant trends between 2012–2017 (19). Alternative hypotheses have been proposed
117 to explain the decline in atmospheric Hg in the Northern Hemisphere (NH) while anthropogenic emissions
118 rise, including increased elemental mercury (Hg⁰) uptake by vegetation (20) and declining Hg emissions
119 from ocean legacy re-emissions due to reduced anthropogenic inputs after the 1970s (21, 22). However,
120 a decline in legacy emissions of Hg is difficult to reconcile with biogeochemical box models, which
121 suggest that legacy Hg emissions generally increase if anthropogenic emissions are constant or
122 increasing (23).

123
124 Here, we perform trend analyses on a compiled NH dataset (1992–2022) of ambient Hg⁰ measurements
125 and conduct biogeochemical box model and GEOS-Chem chemistry-transport model simulations to
126 identify emissions trends that would be compatible with observed concentration trends. We focus on Hg⁰
127 measurements rather than gaseous oxidized mercury (GOM) and wet deposition measurements, as past
128 measurements of GOM may have been biased low (24) and wet deposition is more strongly affected by
129 meteorological variability (25). We derive trends not only in the mean or median changes in Hg⁰, but also
130 in other statistical quantiles (e.g., 95th percentile) using quantile regression, which can provide additional
131 information regarding the drivers of trends.

132 133 **Results and Discussion**

134 **Regional trends in observed Hg⁰ (1992–2022).** We analyzed Hg⁰ data from 51 long-term monitoring
135 stations across the NH (Fig. 1). To calculate trends over wider regions, we aggregated stations based on
136 Intergovernmental Panel on Climate Change (IPCC) regions (26) and calculated overall trends using
137 linear mixed effect modeling (Fig. 2A–K and Table S1). Overall trends for all NH regions except
138 Northwestern North America are declining over the available measurement periods between 1992 and
139 2022, with declines ranging between -0.007 and -0.035 ng m⁻³ yr⁻¹ (concentration units refer to standard
140 temperature and pressure, STP). Northwestern North America (Fig. 2J) is the only NH region to show a
141 positive trend, but this region only includes one measurement site (Little Fox Lake, Yukon, Canada). Two
142 possible hypotheses for the positive trend in Little Fox Lake have been suggested: increasing transport
143 from East Asia or increasing wildfire frequency in Western Canada (12). However, in our analysis, the
144 East Asian region also shows declining Hg⁰ concentrations over 2006–2022 (trend -0.023 ± 0.005 ng m⁻³
145 yr⁻¹) (Fig. 2H). Declines have also been observed in other published shorter term measurement records
146 from China (17, 18, 27, 28). For the regions with more available measurement stations, including Eastern
147 North America (ENA, n = 19) and Northern Europe (NEU, n = 13), we tested a nonlinear method of
148 obtaining an overall regional trend using generalized additive models (GAM) (8). The derived regional
149 trends are robust, as both the linear and nonlinear approaches of deriving regional trends yield similar
150 declines in these regions for 2005–2020 (-0.01 to -0.02 ng m⁻³ yr⁻¹) (Supplemental Information, SI, Fig.

151 S4). We have also calculated similar regional trends when conducting a sensitivity test where the analysis
152 of site data is limited to the 2005–2020 period (SI Fig. S5 and Table S3).

153
154 We find an overall NH Hg⁰ decline of -0.011 ± 0.006 ng m⁻³ yr⁻¹ (± 2 standard deviations) for the period
155 2005–2020 (Fig. 2L), calculated by averaging regional trends (Fig. 2A–K) weighted by the areas of
156 corresponding IPCC regions. By first aggregating site trends by region, we reduce inherent biases from
157 the uneven spatial distribution of sites (i.e., biasing toward the trends of Eastern North America and
158 Europe) (SI Fig. S2). Our results largely agree with a previous trend assessment conducted on data from
159 1990–2014 (7), which found regional declines in Hg⁰ of -0.6 to -2% yr⁻¹ (approximately corresponding to
160 -0.01 to -0.03 ng m⁻³ yr⁻¹). The current work benefits from improved statistical techniques to combine
161 information from multiple sites and a larger number of stations and regions covered in more recent time
162 periods. We have not included an analysis of SH regional trends in the current work due to the sparse
163 coverage of SH long-term monitoring stations (Fig. 1). From published information, two SH monitoring
164 stations (Cape Point, South Africa and Amsterdam Island) do not show significant trends during the
165 2012–2017 period, while Cape Point shows a positive trend of ~ 0.008 ng m⁻³ yr⁻¹ over 2007–2017 (19).
166 As the NH has a wider dataset of Hg⁰ time series and is the principal hemisphere for anthropogenic
167 emissions, we proceed with constraining Hg budget trends based on the NH Hg⁰ trend.

168
169 **Constraining emissions trends for 2005–2020.** We ran 2×10^5 scenarios in a biogeochemical box
170 model for 2005–2020, varying 19 Hg budget parameters including the trends in anthropogenic emissions
171 and releases, the response of legacy emissions to recent and historical anthropogenic inputs, emissions
172 speciation trends, and the atmospheric Hg lifetime (Table S4). Figure 3A compares the distributions of
173 simulated Hg⁰ trends for specific trends in anthropogenic emissions, given the uncertainty ranges of all
174 other factors. Note that emissions fluxes are reported in Mg yr⁻¹, and thus trends in these fluxes are
175 expressed as Mg yr⁻². Our best estimate for the observed 2005–2020 trend in surface NH Hg⁰ is $-0.011 \pm$
176 0.006 ng m⁻³ yr⁻¹. However, to account for potential differences between NH surface and whole
177 troposphere trends (SI Section S3.1) we assumed an extended uncertainty range for NH tropospheric Hg⁰
178 trends from -0.017 to -0.004 ng m⁻³ yr⁻¹ (error bar in Fig. 3A).

179
180 The uncertainty range for observed NH troposphere Hg⁰ trends is compatible (>5% overlap in histogram)
181 only with anthropogenic emission trends that are declining by more than -9 Mg yr⁻² (Fig. 3A). Stronger
182 declines in anthropogenic emissions lead to more overlap between the simulated and observed trend
183 ranges, yet they become more difficult to reconcile with existing bottom-up inventories. Our box modeling
184 analysis is consistent with a previous emissions trend estimate based on 1990–2010 observations (610
185 Mg yr⁻¹ total difference; -30.5 Mg yr⁻² trend) (7). The positive NH anthropogenic emissions trend estimated
186 by the Streets et al. (10) inventory for 2005–2015 (34 Mg yr⁻²), should result in NH Hg⁰ increases on the
187 order of 0.09 ng m⁻³ yr⁻¹, with no overlap in the observed trend range. Other global inventories differ in
188 terms of their temporal coverage, yet the EDGAR v4.tox2 inventory estimates an increase of 54 Mg yr⁻²
189 over 2005–2012 in the NH (9) and the AMAP/UNEP inventory estimates an NH increase of 44 Mg yr⁻²
190 between 2010 and 2015 (5). The EDGAR v8.1_toxHg inventory, which was recently released but remains
191 in draft form for speciation estimates (29), shows an NH increase of 35 Mg yr⁻² for 2005–2020 (Fig. S15),
192 We conclude that current bottom-up inventories of anthropogenic Hg emissions are inconsistent with the
193 declines in observed NH Hg⁰ for 2005–2020.

194
195 Previous studies (21, 22) have hypothesized that NH Hg⁰ may be decreasing due to broad-scale declines
196 in legacy emissions, even as anthropogenic emissions increase or stay constant. However, our
197 biogeochemical box model analysis illustrates that it is very unlikely for legacy emissions to decrease if
198 recent (2005–2020) anthropogenic emissions are not also decreasing. Even if anthropogenic emissions
199 stay constant, legacy emissions will grow due to the increasing supply of Hg (23). This effect means that

200 in the case of an anthropogenic emissions trend of zero, the median predicted Hg^0 trend will be positive
201 due to positive trends in re-emissions (Fig. 3A and Fig. S8B). The trend in anthropogenic emissions must
202 be below -8 Mg yr^{-2} for the median predicted Hg^0 trend to become negative (Fig. S8B). We explored the
203 potential impacts of errors in the historical emission and release inventories on the recent re-emissions
204 trend (Fig. S9). If we assume underestimates in 1970 emissions and releases, when Hg discharges were
205 at their peak (30, 31), the recent re-emissions trend would be more negative (Fig. S9A). However, the
206 degree to which the potential error in 1970 emissions affects the 2005–2020 re-emissions trend is smaller
207 than the impacts of more recent errors (1990, 2000), and a factor of ~ 15 smaller than the influence of
208 contemporary (2005–2020) anthropogenic emissions and releases trends (Figs. S9F and G). Therefore,
209 although historical emissions and releases from earlier decades (>30 years) can affect the recent re-
210 emissions trend, the dominant factor for the recent re-emissions trend will be recent trends (<15 years) in
211 anthropogenic Hg inputs to the environment. Our results take into account the uncertainties in the multiple
212 lifetimes of legacy Hg in the surface environment (Table S4).

213
214 We explored the role of trend drivers other than anthropogenic inputs by repeating the sampling of the
215 box model throughout the parameter space, accounting for additional causes. If the oxidation lifetime of
216 Hg^0 declined between 2005–2020, it can become easier to reconcile the observed Hg^0 decline with
217 positive anthropogenic emissions trends (Fig. 3B). However, the oxidation lifetime of Hg^0 would have to
218 decline by 13% for at least a 5% likelihood of positive anthropogenic emissions trends (i.e., when the
219 oxidation lifetime declines by 13% over 2005–2020, 5% of the simulations that are within the observed
220 NH Hg^0 trend range have positive NH anthropogenic emissions trends). A hemispheric decrease in the
221 oxidation lifetime of this magnitude would be surprising for the 2005–2020 period, as modeling estimates
222 for the methane (CH_4) lifetime suggest only 9% declines over the longer period of 1980–2014, driven by
223 increases in hydroxyl radical (OH) concentrations (32). In addition, the two-step Hg oxidation chemistry
224 will be affected by other oxidants as well, including ozone, bromine radicals, and nitrogen oxides (2, 33–
225 35). A recent study has highlighted the role of anthropogenic short-lived halogens in continental Hg
226 oxidation, with more work required to understand their trends (36). Oxidants impacted by anthropogenic
227 pollution sources have likely trended differently in different regions, and therefore are likely not the main
228 factor between the consistent Hg^0 declines seen across the NH. In the unlikely scenario that increased
229 Hg^0 oxidation rates counteracted constant or increasing anthropogenic emissions to yield negative Hg^0
230 trends, one would still expect to see a positive trend in NH Hg wet deposition. This is because: 1) larger
231 emissions would need to be balanced by larger deposition fluxes; and 2) the accelerated oxidation of Hg^0
232 would lead to more Hg depositing through wet deposition (the major fate of soluble Hg^{II}) rather than dry
233 deposition of Hg^0 . However, previous studies have identified overall declines in wet deposition of Hg over
234 North America (13, 14, 37) and Europe (5).

235
236 Another potential factor is the increase in terrestrial primary production through global greening, which
237 Jiskra et al. (20) estimated increased the NH dry deposition of Hg^0 to vegetation by 140 Mg yr^{-1} between
238 1990 and 2010; this corresponds to a decrease of approximately 13% in their estimated Hg^0 lifetime due
239 to vegetation uptake. However, the NH Hg^0 dry deposition lifetime would have to decline by more than
240 19% between 2005 and 2020 to yield a 5% likelihood of positive anthropogenic emissions trends (Fig.
241 3C). A change of this magnitude to vegetation uptake during 2005–2020 is unrealistic, as our GEOS-
242 Chem simulation for that time period shows only a 3% decline in the Hg^0 dry deposition lifetime due to
243 vegetation changes (Fig. S11). Other climate change factors can play a role in recent legacy emissions
244 trends, like release of Hg from melting permafrost (38), changes to ocean evasion of Hg^0 through
245 warming, acidification, and wind speed changes (39), decreased sea ice coverage allowing further Hg^0
246 evasion (40), and enhanced wildfire emissions (41). These identified climate feedbacks, however, tend to
247 increase legacy Hg re-emissions, and thus could not explain why anthropogenic emissions in bottom-up
248 inventories increase while Hg^0 trends decline. Although further research into these factors is required to

249 reduce uncertainties in recent trend drivers, our conclusion remains that it is very unlikely that NH
250 anthropogenic emissions could have increased or even stayed constant over 2005–2020, with the Hg⁰
251 declines observed over this period in the NH.

252

253 **Spatial and quantile variability of Hg⁰ trends.** Although the box model is useful for constraining overall
254 hemispheric trends, it cannot capture the spatial heterogeneity of these trends driven by variability in
255 sources, sinks, and transport. As these simulations are run with observed meteorology from the MERRA-
256 2 reanalysis product (42), the GEOS-Chem simulations account for interannual variability or potential
257 climate change-driven trends in meteorology for 2005–2020. We ran simulations (Table 1) in the 3-D
258 chemical-transport model GEOS-Chem (43, 44) to investigate different emissions scenarios over the
259 2005–2020 period and calculated mean trends in NH Hg⁰ using area-weighted averaging of observed
260 regions (Fig. 4A). The BASE simulation, including anthropogenic emissions increases according to
261 Streets et al. (10) for 2005–2015 with constant emissions after 2015, shows an increase in NH Hg⁰ of
262 0.006 ng m⁻³ yr⁻¹. In the BASE+LEG simulation, we considered the feedback of legacy emissions to
263 increasing anthropogenic emissions, leading to a stronger increase of 0.010 ng m⁻³ yr⁻¹ in NH Hg⁰.
264 Echoing the box modeling results, we thus find that increases in anthropogenic emissions found in
265 existing inventories is inconsistent with the observed trends in NH Hg⁰, -0.011 ± 0.006 ng m⁻³ yr⁻¹.
266 Replacing Chinese emissions within BASE by the regional inventory trend from Zhang et al. (45), the
267 ZHANG23 simulation shows a slight negative trend in NH Hg⁰ (-0.001 ng m⁻³ yr⁻¹). We simulated two
268 further scenarios for a decreasing NH emissions trend: DEC_ANT_NH, where an additional decline of 23
269 Mg yr⁻² in the NH is imposed on top of the ZHANG23 scenario, and DEC_LEG_ONLY, which considers
270 declining ocean re-emissions of Hg in the NH and SH. Both of these emission scenarios are within
271 uncertainties of the observed trend in mean NH Hg⁰ (DEC_ANT_NH: -0.009 ng m⁻³ yr⁻¹;
272 DEC_LEG_ONLY: -0.012 ng m⁻³ yr⁻¹). Since it is difficult to understand the causes of the Hg⁰ decline
273 based on the mean hemispheric trend alone, we also assess the spatial and quantile variations in trends.

274

275 We use quantile regression to assess trends in the observed median (P50) and 95th percentile (P95)
276 deseasonalized daily Hg⁰ values. Fig. 4B maps the simulated P50 trends in BASE+LEG, showing
277 increasing concentrations across the globe, in disagreement with 8 of the 9 plotted stations (>13 years
278 observed between 2005 and 2020), which show declines. The difference between P95 trends and P50
279 trends (Fig. 4C) correlates with the change in anthropogenic emissions between 2005 and 2020 (Fig.
280 S12). BASE+LEG simulates P95 declining more than P50 in Eastern North America and Central Europe
281 (areas of emissions decreases in the global inventory), while P95 increases more than P50 in East Asia
282 and South Africa (areas of emissions increases). Available high-resolution measurement records confirm
283 the simulated P95 – P50 trends in Eastern North America (Egbert and Kejimkujik) and Europe (Mace
284 Head, Schmücke, and Pallas), yet they also show declines in East Asia (Cape Hedo). In the simulations
285 where Chinese emissions decline between 2005 and 2020 (ZHANG23 and DEC_ANT_NH), the
286 simulated P95 – P50 trends agree with observations at Cape Hedo, showing negative values (Figs. 4E
287 and S12D). In the DEC_LEG_ONLY simulation, declining legacy emissions lead to agreement with the
288 observed P50 NH Hg⁰ trends (Fig. 4F), but the P95 – P50 trends remain similar to BASE+LEG and are
289 opposite in sign to Cape Hedo observations (Fig. 4G). Therefore, despite showing similar P50 trends
290 (Figs. 4D and F) in NH Hg⁰, DEC_ANT_NH and DEC_LEG_ONLY can be distinguished by simulated
291 patterns in quantile trends. The current results support findings from Hg measurement studies in the
292 1990s (46, 47), which suggested that reductions in observed extreme concentrations could be useful
293 indicators for regional emissions changes. Incorporation of quantile trends as constraints in Hg modeling
294 can thus help maximize the information provided by high resolution monitoring stations.

295

296

297

298 Implications for the drivers of atmospheric Hg trends.

299 Observed Hg^0 is generally declining in most NH regions, with an estimated hemispheric trend of $-0.011 \pm$
300 $0.006 \text{ ng m}^{-3} \text{ yr}^{-1}$ for 2005–2020. By testing a large ensemble of parameters using box modeling and
301 comparing with available measurements of atmospheric concentrations, we showed that NH
302 anthropogenic emissions likely declined by more than -140 Mg yr^{-1} (-9 Mg yr^{-2}) over this period (Fig. 3A).
303 This result is at odds with existing anthropogenic emissions inventories (5, 9, 10, 29), which all show NH
304 increases of larger than 34 Mg yr^{-2} . Thus, there is a potential gap of 43 Mg yr^{-2} ($\sim 650 \text{ Mg yr}^{-1}$) between
305 estimated anthropogenic emissions trends from inventories and trends expected from observed Hg^0
306 trends. This gap could quantitatively be impacted (in both directions) by factors like the Hg^0 oxidation
307 lifetime and vegetation sink, yet it is unlikely to be substantially reduced (Fig. 3B–C). Our ZHANG23
308 simulation showed that this gap could be partially explained by incorrect Chinese emissions trends in the
309 global emission inventory, with Chinese national inventories including more detailed information on air
310 pollution control device efficiencies (45, 48, 49). The hypothesis of declining Chinese emissions is
311 supported by the observed decline in P95 Hg^0 concentrations at Cape Hedo (Fig. 4E), along with
312 observed declines in mean Hg^0 values from other East Asian stations (Fig. 2H). However, additional
313 declines in anthropogenic emissions across the NH were necessary to match the magnitude of the
314 observed trend in the DEC_ANT_NH simulation. The gap between inventories and measurement-derived
315 emissions trends could be due to the large uncertainties associated with several anthropogenic emissions
316 sources. For example, ASGM is currently thought to be the largest yet highly uncertain source (globally
317 775 Mg yr^{-1} in 2015) of anthropogenic Hg emissions (10), and estimated trends in this source can differ
318 depending on whether it is estimated to change with time following different proxies such as gold demand
319 or poverty (10, 50). High uncertainties are also linked with emissions from Hg-containing products
320 (globally 436 Mg yr^{-1}) (10), as the magnitudes of historically produced Hg are large ($\sim 1000 \text{ Gg}$) and
321 emissions factors as well as timescales are uncertain (51). Measurement constraints are limited, and our
322 five tested GEOS-Chem simulations are not intended to cover the entire range of uncertainty in emissions
323 scenarios, so we cannot further identify the source types responsible for the discrepancy between
324 emissions inventory and observed trends. Nevertheless, both our box and GEOS-Chem modeling
325 analyses suggest that a decline in legacy emissions in the absence of anthropogenic emissions
326 reductions is unlikely given our understanding of the Hg cycle and measured quantile trends.

327
328 The amount of uncertainty in anthropogenic emissions and biogeochemical cycling of Hg emphasizes the
329 need for continued assessment of inventories and models based on available observations and emerging
330 constraints like Hg isotopes (52). Expansion of current monitoring networks in strategic locations and
331 increased public availability of data would be valuable for trend quantification and attribution to sources.
332 For example, existing SH measurement locations are largely influenced by marine rather than
333 anthropogenic sources (53, 54), with no long-term measurement stations located nearby ASGM activities
334 (Fig. 1). We focused here on trends in Hg^0 in the NH due to the increased prevalence of NH
335 anthropogenic emissions and monitoring, but further monitoring of atmospheric Hg in the SH is essential
336 for constraining trends in Hg sources. For example, major differences between the simulated
337 DEC_ANT_NH and DEC_LEG_ONLY median trends occur in the SH (Fig. 4), but we do not evaluate the
338 accuracy of the simulated SH trends as analysis of SH measurements is out of the scope of the current
339 study. Passive samplers (55) can enable economical Hg monitoring in remote locations, yet active
340 continuous sampling will continue to deliver the benefits of higher time resolution (e.g., atmospheric
341 dynamics, source identification) compared to passive samplers (\sim monthly resolution). Here we showed
342 that the trends in the statistical distribution of Hg^0 , which can only be facilitated by active sampling
343 methods, are a useful indicator of which sources are changing. As more data become available from sites
344 measuring GOM using a new generation of methods with smaller biases (56, 57), it will be possible to
345 analyze long term trends in different fractions of atmospheric Hg, providing further information about
346 source changes. Reduced-form models (58, 59) and tools to produce emissions inventories from

347 socioeconomic data more quickly (60), which have been applied extensively in the climate and air
348 pollution fields, can enable more up-to-date evaluations of the latest Hg trends and drivers. Improvements
349 in Hg models will be essential for further analysis of Hg trends, for example refining the response of
350 legacy re-emissions to anthropogenic emissions scenarios and global change factors. The planned
351 analysis to support the Minamata Convention effectiveness evaluation will advance this approach by
352 investigating the drivers of Hg trends in multiple Hg models (61). As declining atmospheric Hg inputs to
353 ecosystems can directly impact concentrations of Hg in biota (62), understanding the trends in
354 atmospheric Hg burden is essential for better predictions of how Hg pollution will evolve under future
355 regulatory control scenarios and climate change.

356

357 **Materials and Methods**

358 **Atmospheric mercury observations.** Atmospheric mercury (Hg) occurs as different species: the volatile
359 species gaseous elemental mercury (GEM: Hg^0), the soluble, shorter-lived species gaseous oxidized
360 mercury (GOM: Hg^I and Hg^{II}), and particulate-bound mercury (Hg^P). We compiled data from 51 stations
361 which have more than 6 years of measurements of Hg^0 or total gaseous mercury (TGM = Hg^0 + GOM) in
362 the period 1992 to 2022 (Table S1). Measurements reporting TGM are likely more representative of Hg^0
363 due to low biases in capturing GOM (63, 64), and therefore we do not differentiate between TGM and Hg^0
364 measurements. For the main manuscript analysis, we compare modeled Hg^0 quantities to the combined
365 TGM and Hg^0 measurement dataset. As a sensitivity test, we excluded all TGM measurements from the
366 datasets, but found no significant differences in regional trends when analyzing Hg^0 measurements alone
367 (Section S4, Fig. S6). We have also tested whether the trend results are similar if modeled TGM data are
368 analyzed instead of modelled Hg^0 and the differences are minor ($< 0.001 \text{ ng m}^{-3} \text{ yr}^{-1}$). We analyzed data
369 from multiple measurement networks: the US National Atmospheric Deposition Program's (NADP)
370 Atmospheric Mercury Network (AMNet) (65), Environment and Climate Change Canada's network
371 (ECCC) (37), European Monitoring and Evaluation Programme (EMEP) (66), Global Mercury Observation
372 System (GMOS) (67), Ministry of Environment Japan (MOEJ) (15), Ministry of Environment (MOENV)
373 Taiwan (16), and the Experimental Lakes Area (68). We also included a Mauna Loa measurement
374 dataset from the US EPA from 2002 to 2009 (69, 70), which later transitioned into an AMNet site. Most
375 TGM and Hg^0 measurements were made with Tekran Instruments Corporation (Toronto, Canada) Models
376 2537A/B/X systems, which capture ambient Hg by gold trap amalgamation, subsequently thermally
377 desorbing this accumulated Hg to be detected by Cold Vapour Atomic Fluorescence Spectrometry
378 (CVAFS) (70). Two sites in the EMEP network (Iskrba after 2017 and Lahemaa) employed Lumex
379 Instruments (St. Petersburg, Russia) Model RA-915 mercury analyzers, which detect Hg^0 through
380 Zeeman Atomic Absorption Spectrometry using High Frequency Modulated light polarisation (ZAAS-HFM)
381 (71). Before 2017, TGM was measured at Iskrba with Mercury Instruments Analytical Technologies
382 (Karlsfeld, Germany) Model UT-3000 analyzers using cold vapor atomic absorption spectroscopy
383 (CVAAS). All the continuous TGM and Hg^0 measurements are made at 5–15 min intervals, which are
384 averaged and reported hourly. Measurements from Zeppelin Station (before 2000), Birkenes (before
385 2010), Lista, Råö, Bredkälen, Hallahus, and Pallas (the measurements from IVL, Swedish Environmental
386 Research Institute) were made manually with a gold trap sampling technique (72). Data at lower
387 frequencies (manual sites and the Auchencorth Moss and Iskrba timeseries) were used to compute
388 monthly mean statistics for timeseries. At the sites with high-frequency measurements, daily mean values
389 were calculated and used to compute means for all months with at least 10 daily values. All measurement
390 and modeling data for Hg^0 is reported in units of $\text{ng m}^{-3} \text{ yr}^{-1}$ at standard temperature and pressure (STP, 0
391 °C and 1 atm).

392

393 **Statistical methods.** Monthly mean data were deseasonalized before trend analysis by fitting each
394 station timeseries with four harmonic terms (73). In order to achieve a better evidence synthesis from
395 individual site data, we focused our statistical analysis on calculating overall trends from wider regions.

396 We chose to aggregate Hg trends based on the IPCC regions (Fig. 1). These regions are standardly used
 397 in the atmospheric science community and are designed to have consistent climate features (26),
 398 providing advantages over using whole continent or country-based aggregations. There are 61 regions in
 399 total; we analyzed trends for 11 regions in the NH where stations measuring Hg over the long term (> 6
 400 years) were available. We aim to derive regionally representative trends by integrating information from all
 401 data sources, because individual sites might only provide a partial view of regional variations, as they
 402 cover different time periods, come from different measurement networks, include data gaps, and are
 403 potentially exposed to unique local sources and sinks. In previous studies on Hg trends, regional
 404 timeseries have been calculated by averaging all sites that are available in a particular year (7). However,
 405 this approach is biased when sites do not all cover the same time period, since offsets between mean site
 406 concentrations can affect the calculated trend results (SI Section S3.2). To address this heterogeneity, we
 407 explicitly modeled offsets and trend deviations between sites with linear mixed effects (LME) models (73,
 408 74). Using LME models, a time series can be described with terms representing the consensus trend and
 409 intercept for a region (“fixed effect”) and terms representing site-level deviations (“random effect”).
 410 Individual sites were modeled using Eq. 1:

$$411 \quad y_k = a + bt + \alpha_k + \beta_k t \quad (\text{Eq. 1})$$

412 where y_k are deseasonalized monthly mean Hg⁰ values for each site, a is the regional intercept, b is the
 413 regional trend, α_k is the site offset, and β_k is the site deviation in trend. To account for autocorrelation, we
 414 assumed that residual errors for each site follow a first-order autoregressive process (AR(1)). We
 415 calculated these trends using LME modeling in the R package lme4 (74). For the purposes of LME
 416 modeling, EPA and AMNet data for Mauna Loa, as well as Finnish Meteorological Institute (FMI) and
 417 Swedish Environmental Research Institute (IVL) data for Pallas, were treated as different sites (as
 418 different measurement networks may have offsets). We applied LME modeling to the nine NH regions
 419 where multisite data is available. For the two regions (Northwestern North America and the Arctic Ocean)
 420 where only one site is available, we calculated generalized least squares (GLS) trends with AR(1) errors
 421 on deseasonalized monthly mean values. We chose linear approaches for trend analysis as this follows
 422 recommendations for multisite analysis when only a few sites are available for a region (73). We found
 423 consistent results between LME trends and nonlinear trends calculated with generalized additive models
 424 (GAMs) for regions (Eastern North America and Northern Europe) where a larger number of sites (>12)
 425 are available (SI Fig. S4).

426
 427 We weighted regional trends by the areas of the corresponding IPCC regions to calculate the overall NH
 428 trend, which allowed us to compare with box model simulations. The overall NH trend was calculated for
 429 2005–2020, which is the time period with the best availability of data from all 11 regions. The error in the
 430 NH trend was calculated through Monte Carlo sampling of regional trends ± 2 standard deviation.
 431 Analogous trend calculations were performed for GEOS-Chem simulated Hg⁰ values, which showed that
 432 NH trends derived from regional weighted averages were more representative of the true NH surface
 433 trend than averages of all available sites without regional aggregation (SI Fig. S2).

434
 435 For sites where high frequency Hg⁰ measurements were available, we additionally calculated quantile
 436 regression (QR) trends over the 2005–2020 period (75). Other atmospheric chemistry studies (8, 76, 77)
 437 have applied QR, as it enables the quantification of trends not only in the mean values but throughout the
 438 distribution of the observed quantity. Earlier studies have observed heterogeneous changes in the
 439 statistical distribution of atmospheric Hg measurements driven by emissions changes (46, 47), yet these
 440 have not been followed up with more modern statistical techniques. We analyzed deseasonalized daily
 441 mean values at these sites and calculated trends for 5th–95th percentiles, with errors derived using
 442 bootstrapping. We applied the R package quantreg for this analysis (78).

443

444 **Box model simulations.** We used a 3-box model that considers atmospheric Hg⁰ and Hg^{II} in two
 445 tropospheric boxes (NH and SH) and one stratospheric box (79) to simulate potential scenarios for trends
 446 during 2005–2020. We constructed an ensemble of scenarios accounting for uncertainties in the
 447 atmospheric Hg lifetime, historical (pre-2005) anthropogenic emissions and releases, recent (2005–2020)
 448 anthropogenic emissions and releases, the response of legacy emissions to anthropogenic inputs, and
 449 recent (2005–2020) speciation trends. We assigned uncertainty ranges to these 19 parameters (SI Table
 450 S4) and sampled 2×10^5 scenarios within this parameter space, using Latin Hypercube Sampling (80).

451
 452 To address the response in legacy emissions to historical and recent anthropogenic inputs, we applied
 453 the effective anthropogenic mercury deposition (EAMD) concept (81). Our approach used two minor
 454 adaptations: (1) tracking the effective anthropogenic mercury emissions (EAME) instead of deposition
 455 (which leads to offsets of several months in lifetimes); and (2) using a two-term negative exponential
 456 model. Given primary emissions or releases of mercury in a specific year (ϵ_i), Eq. 2 calculates the EAME,
 457 in a future time t :

$$458 \quad \text{EAME}_i(t) = \epsilon_i \left(a_1 \exp\left(-\frac{t}{b_1}\right) + a_2 \exp\left(-\frac{t}{b_2}\right) \right) \quad (\text{Eq. 2})$$

459
 460 where a_1 and a_2 are coefficients and b_1 and b_2 are lifetimes representing the quick and slow re-emission
 461 processes, respectively. Total legacy emissions (E_{leg}) in the year t were calculated by summing up all
 462 EAME_i resulting from previous primary emissions using Eq. 3:

$$463 \quad E_{\text{leg}}(t) = \sum_{i < t} \text{EAME}_i \quad (\text{Eq. 3})$$

464
 465 We employed pulse experiments with parameter perturbations in the Hg Global Biogeochemical Box
 466 model (GBC) (6, 82) to calculate reasonable ranges for the a and b parameters (SI Section S5). We
 467 pulsed an additional 100 Mg Hg either emitted or released to rivers in 2010 and fit the resultant additional
 468 legacy re-emissions until 2110 using Eq. 2. We conducted these pulse experiments on 1000 iterations of
 469 the GBC model, varying each of the 40 rate coefficients and parameters within the GBC model within a
 470 factor of 2 using Latin Hypercube Sampling. We found that b_1 ranges between 6–15 months for
 471 atmospheric emissions and 2–10 months for releases, corresponding to the timescale of atmospheric
 472 deposition and re-emission from the surface ocean. The longer lifetime, b_2 , ranges between 29–97 years
 473 for atmospheric emissions and 1–117 years for releases, corresponding to the timescale of removal of Hg
 474 from the atmosphere–surface ocean–subsurface ocean system through transfer to the deep ocean or
 475 temporary storage in soils (6). We calculated ranges for the fraction of Hg re-emitted in the short
 476 timescale term and the total Hg re-emissions resulting from a pulse, which can be used to calculate a_1
 477 and a_2 in Eq. 2. Although longer time scales (~1000 yr) would be required to model burial of Hg in the
 478 deep ocean, Eq. 2 covers the legacy re-emission response in near-future projections (<100 years), while
 479 having only 4 parameters as opposed to 40 parameters in the GBC model (81).

480
 481
 482 Anthropogenic emissions and releases of Hg were taken from the Streets et al. (31) inventory, which
 483 covers decadal points over the historical period (1510–2010). We accounted for uncertainties in
 484 emissions and releases for recent decadal points (1970, 1980, 1990, 2000, 2010) by applying
 485 perturbations between –20% and +40% to these values, which is the suggested emission inventory
 486 uncertainty range (10). We interpolated between the decadal points to calculate emissions with yearly
 487 resolution between 1510–2005. For 2005–2020, we applied varying linear trends in anthropogenic
 488 emissions for both hemispheres, restricting the trend range to ensure non-negative emissions in 2020.
 489 The anthropogenic releases for 2005–2020 were calculated based on the historical relationship between
 490 emissions and releases trends in the inventory (31), with random perturbations introduced for the
 491 hemispheric release trends (Table S4). This procedure yielded 2×10^5 potential timeseries for

492 anthropogenic emissions and releases over 1510–2020. Combining these scenarios with varying sets of
493 legacy parameters (Eq. 2), we calculated the resultant global legacy re-emissions timeseries for 2005–
494 2020 for each of the 2×10^5 scenarios. For simplicity, the distribution of legacy re-emissions by
495 hemisphere was assumed to be constant over 2005–2020 based on the ratio in GEOS-Chem (44% NH,
496 55% SH; this is similar to the ratio of ocean coverage in the NH and SH). Speciation of the anthropogenic
497 emissions in 2005 was set to 65% Hg^0 and 35% Hg^{II} ; we applied a variable linear trend in speciation so
498 that speciation in 2020 ranged between 45% and 85% Hg^0 .

499
500 We ran the 2×10^5 scenarios in the 3-box model for 2005 to evaluate whether the sampled combinations
501 of emissions and atmospheric Hg lifetimes (ranging between 3–8 months) yield a reasonable Hg burden.
502 We rejected scenarios that yield a 2005 burden in the NH troposphere outside of the range 1600–3300
503 Mg (corresponding to average tropospheric concentrations of 0.8–1.6 ng m^{-3}). Approximately 10^5 samples
504 passed this constraint, which we then utilized for full 2005–2020 box model runs. We evaluated linear
505 trends in NH Hg^0 in each of these box model runs and compared these to the inputted total and
506 anthropogenic emission trends for 2005–2020.

507
508 To assess the impacts of other non-emissions factors in NH Hg^0 trends, we repeated this procedure
509 accounting for potential trends in Hg^0 dry deposition and oxidation. We re-ran the 2×10^5 scenarios with
510 linear trends in the dry deposition rate coefficient so that the value in 2020 varied between 100% to 170%
511 of its value in 2005. Similarly, we ran 2×10^5 scenarios with the Hg^0 oxidation rate coefficient varying in
512 2020 between 100% and 200% of its value in 2005.

513
514 **GEOS-Chem simulations.** We ran 3-D atmospheric simulations for the 2005–2020 period in the
515 chemistry-transport model GEOS-Chem. We used version 12.8.1 of the Hg model (43) with improvements
516 in the dry deposition of Hg^0 (79). The model was run globally at $2.0^\circ \times 2.5^\circ$ horizontal resolution and 47
517 vertical levels up to 0.01 hPa (80 km). The model was forced with offline meteorology from the MERRA-2
518 product (42). The model treats three species of Hg: elemental mercury (Hg^0), oxidized mercury (Hg^{II} ,
519 GOM), and particulate mercury (Hg^{P}). Oxidation of Hg^0 occurs through a two-step mechanism initiated by
520 atomic bromine (Br), while photoreduction of Hg^{II} occurs in the aqueous phase as a function of the NO_2
521 photolysis rate and organic aerosol concentrations (43). The reduction rate coefficient ($K_{\text{RED_JNO2}}$)
522 was set to $2.4 \text{ m}^{-3} \mu\text{g}^{-1}$ so that modeled Hg^0 concentrations agree with observed values in 2005. The Hg
523 chemistry in GEOS-Chem has been updated in more recent model versions (v14 onwards), yet the
524 overall atmospheric lifetime and transport of Hg remain similar (2) and the faster computational speed of
525 v12.8.1 facilitates these 16-year simulations. Legacy re-emissions of Hg from the ocean are calculated
526 online (depending on temperature and wind speed) through an air-sea exchange parametrization (83),
527 with concentrations of Hg in the surface ocean taken from a previous ocean general circulation model
528 (MITgcm) simulation (43). Soil legacy emissions are parametrized depending on solar radiation,
529 vegetation cover, and concentrations of Hg in soil (84). The model also considers prompt recycling of Hg^{II}
530 deposited to soils and snow (85), geogenic emissions of Hg^0 (44), and transient emissions of Hg^0 from
531 biomass burning based on GFED v4.1s (86). More comprehensive descriptions of this version of the
532 GEOS-Chem Hg model can be found elsewhere (43, 79).

533
534 Five simulations (Table 1) were performed to evaluate spatial heterogeneity in atmospheric Hg trends
535 under different emissions scenarios (SI Fig. S10), which are intended to be illustrative but do not cover
536 the full range of potential scenarios. The BASE case used Streets et al. (10) anthropogenic emissions of
537 Hg for 2005–2015, with 2016–2020 retaining the same emissions pattern as 2015. The BASE+LEG
538 simulation additionally considered the median box modeled trend (Fig. S9F) in NH legacy emissions ($+14$
539 Mg yr^{-2}) due to the BASE trend in NH anthropogenic emissions ($+23 \text{ Mg yr}^{-2}$) over 2005–2020. This trend
540 in legacy emissions was fully ascribed to the ocean through scaling oceanic sea surface concentrations of

541 Hg (43) to yield the NH trend in legacy emissions. In the ZHANG23 scenario, we replaced the trend in
 542 Chinese emissions from BASE with the national inventory in Zhang et al. (45). To distribute Chinese
 543 emissions in a consistent way with the Streets et al. (10) inventory, we scaled the emissions for 2005–
 544 2020 using the equation:

$$546 \quad E_{\text{ZHANG23}}^{i'} = E_{\text{BASE}}^i \times \frac{E_{\text{ZHANG23}}^i}{E_{\text{ZHANG23}}^{2005}} \quad (\text{Eq. 4})$$

547 where $E_{\text{ZHANG23}}^{i'}$ are the distributed Chinese emissions applied in the ZHANG23 simulation for year i ,
 548 E_{BASE}^i are the Chinese emissions applied in the BASE, E_{ZHANG23}^i are the total Chinese emissions for a
 549 specific year in the Zhang et al. (45) inventory, and $E_{\text{ZHANG23}}^{2005}$ are the total Chinese emissions in the Zhang
 550 et al. (45) inventory for 2005. In this way, the normalized China trend for 2005–2020 is taken from the
 551 Zhang et al. (45), but emissions magnitudes differ due to differences in 2005 total Chinese emissions
 552 between BASE (701 Mg yr⁻¹) and Zhang et al. (45) (466 Mg yr⁻¹). We also adjusted the ZHANG23 trend in
 553 NH legacy emissions (+4 Mg yr⁻²) by scaling ocean concentrations so that it is coherent with the NH
 554 anthropogenic emissions trend (-11 Mg yr⁻²) (Fig. S9F).
 555

556 To develop a scenario with declining anthropogenic emissions that would be compatible with observed
 557 NH Hg⁰ trends (DEC_ANT_NH), we imposed an additional 23 Mg yr⁻² decline for 2005–2020 in the NH.
 558 Anthropogenic Hg emissions outside of China were scaled uniformly by year so that the decline is 23 Mg
 559 yr⁻² more than in ZHANG23, for a total anthropogenic trend of -34 Mg yr⁻² (Table 1). NH legacy emissions
 560 (-2 Mg yr⁻²) were adjusted to be consistent with the DEC_ANT_NH trend in anthropogenic emissions. As
 561 a fifth scenario, we explored the possibility where anthropogenic emissions follow BASE, but a major
 562 decline (-50 Mg yr⁻²) in NH ocean legacy emissions occurs (DEC_LEG_ONLY). Thus, the mean NH
 563 trends in Hg⁰ are similar between DEC_ANT_NH and DEC_LEG_ONLY (Fig. 4A), but the source
 564 contribution and spatial distribution varies. In addition, while DEC_ANT_NH includes stagnant overall SH
 565 emissions (-2 Mg yr⁻²), DEC_LEG_ONLY has SH emissions declines (-74 Mg yr⁻²) due to the scaling of
 566 ocean concentrations.
 567

568 Acknowledgments

569 This work was funded by the Swiss National Science Foundation through an Early Postdoc.Mobility grant
 570 to A.F. (P2EZP2_195424) and a grant (#1924148) from the US National Science Foundation to N.E.S.
 571 The EPA (<https://catalog.data.gov/dataset/epa-sciencehub>) through its Office of Research and
 572 Development partially funded and contributed to this research. The views expressed in this paper are
 573 those of the authors and do not necessarily reflect the views or policies of EPA. It has been subjected to
 574 Agency review and approved for publication. Mention of trade names or commercial products do not
 575 constitute an endorsement or recommendation for use. The authors acknowledge Environment and
 576 Climate Change Canada ([https://www.canada.ca/en/environment-climate-change/services/air-
 577 pollution/monitoring-networks-data/canadian-air-precipitation.html](https://www.canada.ca/en/environment-climate-change/services/air-pollution/monitoring-networks-data/canadian-air-precipitation.html)), the NADP Atmospheric Mercury
 578 Network (AMNet) (<https://nadp.slh.wisc.edu/networks/atmospheric-mercury-network/>), New York State
 579 Department of Environmental Conservation, European Monitoring and Evaluation Programme (EMEP)
 580 (<https://ebas-data.nilu.no>), Global Mercury Observation System (GMOS) (<https://sdi.iaa.cnr.it/gos4mcat>),
 581 Ministry of Environment Japan (MOEJ) (<https://www.env.go.jp/en/chemi/mcm/monitoringdb2.html>),
 582 Ministry of Environment (MOENV) Taiwan, and IISD Experimental Lakes Area (<https://www.iisd.org/ela>)
 583 for the provision of atmospheric mercury data. The authors would like to acknowledge the following for
 584 the funding of the Auchencorth Moss UK site, the UK Department for Environment, Food and Rural
 585 Affairs (Defra) and the devolved administrations, via the UK Eutrophying and Acidifying Atmospheric
 586 Pollutants (UKEAP) contract and by the Natural Environmental Research Council (NERC) National
 587

588 Capability UK-SCaPE programme. K.-L.C. is supported by NOAA cooperative agreement
589 NA22OAR4320151. We would like to thank David Gay and Ralf Ebinghaus for helpful discussion about
590 available Hg measurements.

591

592 **Code and Data Availability**

593 Model code, analysis scripts, and all data to reproduce figures and analyses are published in Zenodo

594 (<https://doi.org/10.5281/zenodo.13618039>) under a CC BY 4.0 license

595 (<https://creativecommons.org/licenses/by/4.0/>).

596

597 **References**

- 598 1. UNTC, Minamata Convention on Mercury (2013).
599 2. V. Shah, *et al.*, Improved Mechanistic Model of the Atmospheric Redox Chemistry of Mercury.
600 *Environ. Sci. Technol.* **55**, 14445–14456 (2021).
601 3. UNEP/MC/COP.3, “Proposed indicators for evaluating the effectiveness of the Minamata
602 Convention, by article. Annex I to decision MC-3/10.” (2020).
603 4. F. Steenhuisen, S. J. Wilson, Development and application of an updated geospatial distribution
604 model for gridding 2015 global mercury emissions. *Atmos. Environ.* **211**, 138–150 (2019).
605 5. UNEP, *Global Mercury Assessment 2018* (UN Environment Programme, Chemicals and Health
606 Branch. Geneva, Switzerland, 2019).
607 6. H. M. Amos, D. J. Jacob, D. G. Streets, E. M. Sunderland, Legacy impacts of all-time anthropogenic
608 emissions on the global mercury cycle. *Global Biogeochem. Cycles* **27**, 410–421 (2013).
609 7. Y. Zhang, *et al.*, Observed decrease in atmospheric mercury explained by global decline in
610 anthropogenic emissions. *Proc. Natl. Acad. Sci. U.S.A.* **113**, 526–531 (2016).
611 8. K.-L. Chang, *et al.*, Trend detection of atmospheric time series. *Elementa: Science of the*
612 *Anthropocene* **9**, 00035 (2021).
613 9. M. Muntean, *et al.*, Evaluating EDGARv4.tox2 speciated mercury emissions ex-post scenarios and
614 their impacts on modelled global and regional wet deposition patterns. *Atmospheric Environment*
615 **184**, 56–68 (2018).
616 10. D. G. Streets, *et al.*, Global and regional trends in mercury emissions and concentrations, 2010–
617 2015. *Atmospheric Environment* **201**, 417–427 (2019).
618 11. D. Custódio, *et al.*, Odds and ends of atmospheric mercury in Europe and over the North Atlantic
619 Ocean: temporal trends of 25 years of measurements. *Atmos. Chem. Phys.* **22**, 3827–3840 (2022).
620 12. K. MacSween, *et al.*, Updated trends for atmospheric mercury in the Arctic: 1995–2018. *Science of*
621 *The Total Environment* **837**, 155802 (2022).
622 13. C. I. Olson, H. Fakhraei, C. T. Driscoll, Mercury Emissions, Atmospheric Concentrations, and Wet
623 Deposition across the Conterminous United States: Changes over 20 Years of Monitoring. *Environ.*
624 *Sci. Technol. Lett.* **7**, 376–381 (2020).
625 14. P. S. Weiss-Penzias, *et al.*, Trends in mercury wet deposition and mercury air concentrations across
626 the U.S. and Canada. *Science of The Total Environment* **568**, 546–556 (2016).
627 15. K. Marumoto, *et al.*, Long-Term Observation of Atmospheric Speciated Mercury during 2007–2018
628 at Cape Hedo, Okinawa, Japan. *Atmosphere* **10**, 362 (2019).
629 16. L. S. P. Nguyen, G.-R. Sheu, D.-W. Lin, N.-H. Lin, Temporal changes in atmospheric mercury
630 concentrations at a background mountain site downwind of the East Asia continent in 2006–2016.
631 *Science of The Total Environment* **686**, 1049–1056 (2019).
632 17. J. Shi, *et al.*, Measurement report: Atmospheric mercury in a coastal city of Southeast China – inter-
633 annual variations and influencing factors. *Atmos. Chem. Phys.* **22**, 11187–11202 (2022).
634 18. Q. Wu, *et al.*, Developing a statistical model to explain the observed decline of atmospheric
635 mercury. *Atmospheric Environment* **243**, 117868 (2020).
636 19. F. Slemr, *et al.*, Atmospheric mercury in the Southern Hemisphere – Part 1: Trend and inter-annual
637 variations in atmospheric mercury at Cape Point, South Africa, in 2007–2017, and on Amsterdam
638 Island in 2012–2017. *Atmos. Chem. Phys.* **20**, 7683–7692 (2020).
639 20. M. Jiskra, *et al.*, A vegetation control on seasonal variations in global atmospheric mercury
640 concentrations. *Nature Geosci* **11**, 244–250 (2018).
641 21. F. Slemr, E.-G. Brunke, R. Ebinghaus, J. Kuss, Worldwide trend of atmospheric mercury since
642 1995. *Atmos. Chem. Phys.* **11**, 4779–4787 (2011).
643 22. A. L. Soerensen, *et al.*, Multi-decadal decline of mercury in the North Atlantic atmosphere explained
644 by changing subsurface seawater concentrations. *Geophys. Res. Lett.* **39** (2012).
645 23. H. Angot, *et al.*, Global and Local Impacts of Delayed Mercury Mitigation Efforts. *Environ. Sci.*
646 *Technol.* **52**, 12968–12977 (2018).
647 24. S. N. Lyman, L. E. Gratz, S. M. Dunham-Cheatham, M. S. Gustin, A. Luippold, Improvements to the
648 Accuracy of Atmospheric Oxidized Mercury Measurements. *Environ. Sci. Technol.* **54**, 13379–
649 13388 (2020).
650 25. A. Giang, *et al.*, Understanding factors influencing the detection of mercury policies in modelled
651 Laurentian Great Lakes wet deposition. *Environ. Sci.: Processes Impacts* **20**, 1373–1389 (2018).

- 652 26. M. Iturbide, *et al.*, An update of IPCC climate reference regions for subcontinental analysis of
653 climate model data: definition and aggregated datasets. *Earth Syst. Sci. Data* **12**, 2959–2970
654 (2020).
- 655 27. Y. Tang, *et al.*, Recent decrease trend of atmospheric mercury concentrations in East China: the
656 influence of anthropogenic emissions. *Atmos. Chem. Phys.* **18**, 8279–8291 (2018).
- 657 28. P. Sun, *et al.*, Declines of gaseous element mercury concentrations at an urban site in eastern
658 China caused by reductions of anthropogenic emission. *Atmospheric Environment* **317**, 120199
659 (2024).
- 660 29. M. Muntean, *et al.*, EDGAR v8.1 Global Mercury Emissions. European Commission, Joint Research
661 Centre (JRC) [Dataset] PID: <http://data.europa.eu/89h/83b507d7-5218-4dc5-95f9-0ec36f073204>.
662 Deposited 2024.
- 663 30. H. Selin, N. E. Selin, From Stockholm to Minamata and beyond: Governing mercury pollution for a
664 more sustainable future. *One Earth* **5**, 1109–1125 (2022).
- 665 31. D. G. Streets, *et al.*, Five hundred years of anthropogenic mercury: spatial and temporal release
666 profiles. *Environ. Res. Lett.* **14**, 084004 (2019).
- 667 32. D. S. Stevenson, *et al.*, Trends in global tropospheric hydroxyl radical and methane lifetime since
668 1850 from AerChemMIP. *Atmos. Chem. Phys.* **20**, 12905–12920 (2020).
- 669 33. T. S. Dibble, H. L. Tetu, Y. Jiao, C. P. Thackray, D. J. Jacob, Modeling the OH-Initiated Oxidation of
670 Mercury in the Global Atmosphere without Violating Physical Laws. *J. Phys. Chem. A* **124**, 444–453
671 (2020).
- 672 34. J. P. Parrella, *et al.*, Tropospheric bromine chemistry: implications for present and pre-industrial
673 ozone and mercury. *Atmos. Chem. Phys.* **12**, 6723–6740 (2012).
- 674 35. A. Saiz-Lopez, *et al.*, Photochemistry of oxidized Hg(I) and Hg(II) species suggests missing mercury
675 oxidation in the troposphere. *Proc. Natl. Acad. Sci. U.S.A.* **117**, 30949–30956 (2020).
- 676 36. X. Fu, *et al.*, Anthropogenic short-lived halogens increase human exposure to mercury
677 contamination due to enhanced mercury oxidation over continents. *Proc. Natl. Acad. Sci. U.S.A.*
678 **121**, e2315058121 (2024).
- 679 37. A. Cole, *et al.*, A Survey of Mercury in Air and Precipitation across Canada: Patterns and Trends.
680 *Atmosphere* **5**, 635–668 (2014).
- 681 38. K. Schaefer, *et al.*, Potential impacts of mercury released from thawing permafrost. *Nat Commun*
682 **11**, 4650 (2020).
- 683 39. Y. Wang, P. Wu, Y. Zhang, Climate-driven changes of global marine mercury cycles in 2100. *Proc.*
684 *Natl. Acad. Sci. U.S.A.* **120**, e2202488120 (2023).
- 685 40. B. P. DiMento, R. P. Mason, S. Brooks, C. Moore, The impact of sea ice on the air-sea exchange of
686 mercury in the Arctic Ocean. *Deep Sea Research Part I: Oceanographic Research Papers* **144**, 28–
687 38 (2019).
- 688 41. A. Kumar, S. Wu, Y. Huang, H. Liao, J. O. Kaplan, Mercury from wildfires: Global emission
689 inventories and sensitivity to 2000–2050 global change. *Atmospheric Environment* **173**, 6–15
690 (2018).
- 691 42. R. Gelaro, *et al.*, The Modern-Era Retrospective Analysis for Research and Applications, Version 2
692 (MERRA-2). *J. Clim.* **30**, 5419–5454 (2017).
- 693 43. H. M. Horowitz, *et al.*, A new mechanism for atmospheric mercury redox chemistry: implications for
694 the global mercury budget. *Atmos. Chem. Phys.* **17**, 6353–6371 (2017).
- 695 44. N. E. Selin, *et al.*, Chemical cycling and deposition of atmospheric mercury: Global constraints from
696 observations. *J. Geophys. Res.* **112**, D02308 (2007).
- 697 45. Y. Zhang, *et al.*, Improved Anthropogenic Mercury Emission Inventories for China from 1980 to
698 2020: Toward More Accurate Effectiveness Evaluation for the Minamata Convention. *Environ. Sci.*
699 *Technol.* **57**, 8660–8670 (2023).
- 700 46. Å. Iverfeldt, J. Munthe, C. Brosset, J. Pacyna, “Long-Term Changes in Concentration and
701 Deposition of Atmospheric Mercury Over Scandinavia” in *Mercury as a Global Pollutant:*
702 *Proceedings of the Third International Conference Held in Whistler, British Columbia, July 10–14,*
703 *1994*, D. B. Porcella, J. W. Huckabee, B. Wheatley, Eds. (Springer Netherlands, 1995), pp. 227–
704 233.
- 705 47. F. Slemr, H. E. Scheel, Trends in atmospheric mercury concentrations at the summit of the Wank
706 mountain, southern Germany. *Atmospheric Environment* **32**, 845–853 (1998).

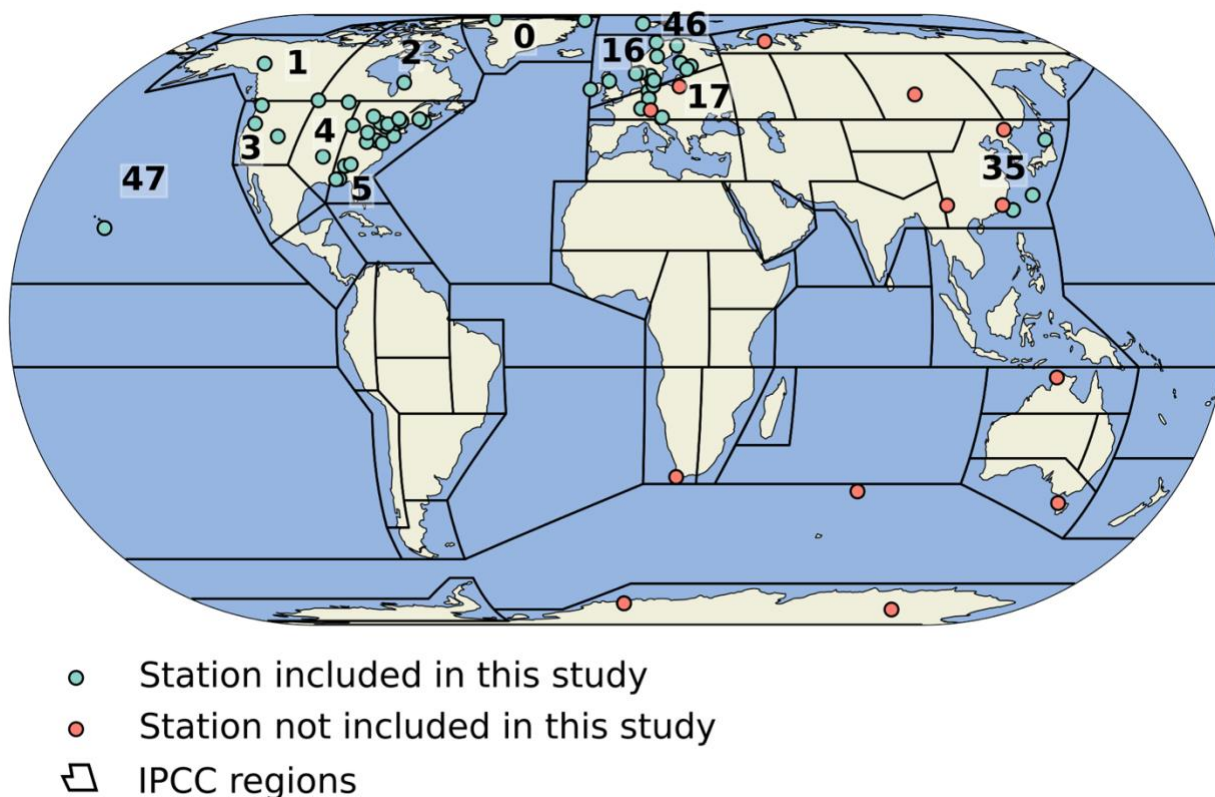
- 707 48. K. Liu, *et al.*, Measure-Specific Effectiveness of Air Pollution Control on China's Atmospheric
708 Mercury Concentration and Deposition during 2013–2017. *Environ. Sci. Technol.* **53**, 8938–8946
709 (2019).
- 710 49. Q. Wu, *et al.*, Temporal Trend and Spatial Distribution of Speciated Atmospheric Mercury Emissions
711 in China During 1978–2014. *Environ. Sci. Technol.* **50**, 13428–13435 (2016).
- 712 50. M. Muntean, *et al.*, Trend analysis from 1970 to 2008 and model evaluation of EDGARv4 global
713 gridded anthropogenic mercury emissions. *Science of The Total Environment* **494–495**, 337–350
714 (2014).
- 715 51. H. M. Horowitz, D. J. Jacob, H. M. Amos, D. G. Streets, E. M. Sunderland, Historical Mercury
716 Releases from Commercial Products: Global Environmental Implications. *Environ. Sci. Technol.* **48**,
717 10242–10250 (2014).
- 718 52. S. Y. Kwon, *et al.*, Mercury stable isotopes for monitoring the effectiveness of the Minamata
719 Convention on Mercury. *Earth-Science Reviews* **203**, 103111 (2020).
- 720 53. J. A. Fisher, *et al.*, A synthesis of mercury research in the Southern Hemisphere, part 2:
721 Anthropogenic perturbations. *Ambio* **52**, 918–937 (2023).
- 722 54. L. Schneider, *et al.*, A synthesis of mercury research in the Southern Hemisphere, part 1: Natural
723 processes. *Ambio* **52**, 897–917 (2023).
- 724 55. D. S. McLagan, *et al.*, A High-Precision Passive Air Sampler for Gaseous Mercury. *Environ. Sci.*
725 *Technol. Lett.* **3**, 24–29 (2016).
- 726 56. S. M. Dunham-Cheatham, S. Lyman, M. S. Gustin, Comparison and calibration of methods for
727 ambient reactive mercury quantification. *Science of The Total Environment* **856**, 159219 (2023).
- 728 57. A. Luippold, *et al.*, Use of Multiple Lines of Evidence to Understand Reactive Mercury
729 Concentrations and Chemistry in Hawai'i, Nevada, Maryland, and Utah, USA. *Environ. Sci. Technol.*
730 **54**, 7922–7931 (2020).
- 731 58. F. De Simone, *et al.*, A Chemical Transport Model Emulator for the Interactive Evaluation of Mercury
732 Emission Reduction Scenarios. *Atmosphere* **11**, 878 (2020).
- 733 59. C. W. Tessum, J. D. Hill, J. D. Marshall, InMAP: A model for air pollution interventions. *PLoS ONE*
734 **12**, e0176131 (2017).
- 735 60. W. Atkinson, *et al.*, A tool for air pollution scenarios (TAPS v1.0) to enable global, long-term, and
736 flexible study of climate and air quality policies. *Geosci. Model Dev.* **15**, 7767–7789 (2022).
- 737 61. A. Dastoor, *et al.*, The Multi-Compartment Hg Modeling and Analysis Project (MCHgMAP): Mercury
738 modeling to support international environmental policy. *Geoscientific Model Development*
739 *Discussions* **2024**, 1–171 (2024).
- 740 62. P. J. Blanchfield, *et al.*, Experimental evidence for recovery of mercury-contaminated fish
741 populations. *Nature* **601**, 74–78 (2022).
- 742 63. A. Steffen, *et al.*, A synthesis of atmospheric mercury depletion event chemistry in the atmosphere
743 and snow. *Atmospheric Chemistry and Physics* **8**, 1445–1482 (2008).
- 744 64. M. S. Gustin, *et al.*, Do We Understand What the Mercury Speciation Instruments Are Actually
745 Measuring? Results of RAMIX. *Environ. Sci. Technol.* **47**, 7295–7306 (2013).
- 746 65. D. A. Gay, *et al.*, The Atmospheric Mercury Network: measurement and initial examination of an
747 ongoing atmospheric mercury record across North America. *Atmos. Chem. Phys.* **13**, 11339–11349
748 (2013).
- 749 66. K. Tørseth, *et al.*, Introduction to the European Monitoring and Evaluation Programme (EMEP) and
750 observed atmospheric composition change during 1972–2009. *Atmos. Chem. Phys.* **12**, 5447–5481
751 (2012).
- 752 67. F. Sprovieri, *et al.*, Atmospheric mercury concentrations observed at ground-based monitoring sites
753 globally distributed in the framework of the GMOS network. *Atmos. Chem. Phys.* **16**, 11915–11935
754 (2016).
- 755 68. V. L. St. Louis, *et al.*, Atmospheric Concentrations and Wet/Dry Loadings of Mercury at the Remote
756 Experimental Lakes Area, Northwestern Ontario, Canada. *Environ. Sci. Technol.* **53**, 8017–8026
757 (2019).
- 758 69. F. Carbone, *et al.*, Sea surface temperature variation linked to elemental mercury concentrations
759 measured on Mauna Loa. *Geophys. Res. Lett.* **43**, 7751–7757 (2016).
- 760 70. M. S. Landis, R. K. Stevens, F. Schaedlich, E. M. Prestbo, Development and Characterization of an
761 Annular Denuder Methodology for the Measurement of Divalent Inorganic Reactive Gaseous
762 Mercury in Ambient Air. *Environ. Sci. Technol.* **36**, 3000–3009 (2002).

- 763 71. S. Sholupov, S. Pogarev, V. Ryzhov, N. Mashyanov, A. Stroganov, Zeeman atomic absorption
764 spectrometer RA-915+ for direct determination of mercury in air and complex matrix samples. *Fuel*
765 *Processing Technology* **85**, 473–485 (2004).
766 72. Å. Iverfeldt, Occurrence and turnover of atmospheric mercury over the nordic countries. *Water, Air,*
767 *and Soil Pollution* **56**, 251–265 (1991).
768 73. K.-L. Chang, M. G. Schultz, G. Koren, Selke, Niklas, Guidance note on best statistical practices for
769 TOAR analyses. Available at: <https://doi.org/10.48550/arXiv.2304.14236>. (2023).
770 74. D. Bates, M. Mächler, B. Bolker, S. Walker, Fitting Linear Mixed-Effects Models Using *lme4*. *J. Stat.*
771 *Soft.* **67** (2015).
772 75. R. Koenker, K. F. Hallock, Quantile Regression. *The Journal of Economic Perspectives* **15**, 143–
773 156 (2001).
774 76. K.-L. Chang, *et al.*, Impact of the COVID-19 Economic Downturn on Tropospheric Ozone Trends:
775 An Uncertainty Weighted Data Synthesis for Quantifying Regional Anomalies Above Western North
776 America and Europe. *AGU Advances* **3**, e2021AV000542 (2022).
777 77. W. C. Porter, C. L. Heald, D. Cooley, B. Russell, Investigating the observed sensitivities of air-
778 quality extremes to meteorological drivers via quantile regression. *Atmos. Chem. Phys.* **15**, 10349–
779 10366 (2015).
780 78. R. Koenker, quantreg: Quantile Regression. Available at: [https://CRAN.R-](https://CRAN.R-project.org/package=quantreg)
781 [project.org/package=quantreg](https://CRAN.R-project.org/package=quantreg). (2022).
782 79. A. Feinberg, T. Dlamini, M. Jiskra, V. Shah, N. E. Selin, Evaluating atmospheric mercury (Hg)
783 uptake by vegetation in a chemistry-transport model. *Environ. Sci.: Processes Impacts* **24**, 1303–
784 1318 (2022).
785 80. M. D. McKay, R. J. Beckman, W. J. Conover, Comparison of Three Methods for Selecting Values of
786 Input Variables in the Analysis of Output from a Computer Code. *Technometrics* **21**, 239–245
787 (1979).
788 81. N. E. Selin, A proposed global metric to aid mercury pollution policy. *Science* **360**, 607–609 (2018).
789 82. H. M. Amos, *et al.*, Global Biogeochemical Implications of Mercury Discharges from Rivers and
790 Sediment Burial. *Environ. Sci. Technol.* **48**, 9514–9522 (2014).
791 83. P. D. Nightingale, *et al.*, In situ evaluation of air-sea gas exchange parameterizations using novel
792 conservative and volatile tracers. *Global Biogeochem. Cycles* **14**, 373–387 (2000).
793 84. S. Song, *et al.*, Top-down constraints on atmospheric mercury emissions and implications for global
794 biogeochemical cycling. *Atmos. Chem. Phys.* **15**, 7103–7125 (2015).
795 85. N. E. Selin, *et al.*, Global 3-D land-ocean-atmosphere model for mercury: Present-day versus
796 preindustrial cycles and anthropogenic enrichment factors for deposition. *Global Biogeochem.*
797 *Cycles* **22**, GB2011 (2008).
798 86. G. R. van der Werf, *et al.*, Global fire emissions estimates during 1997–2016. *Earth Syst. Sci. Data*
799 **9**, 697–720 (2017).

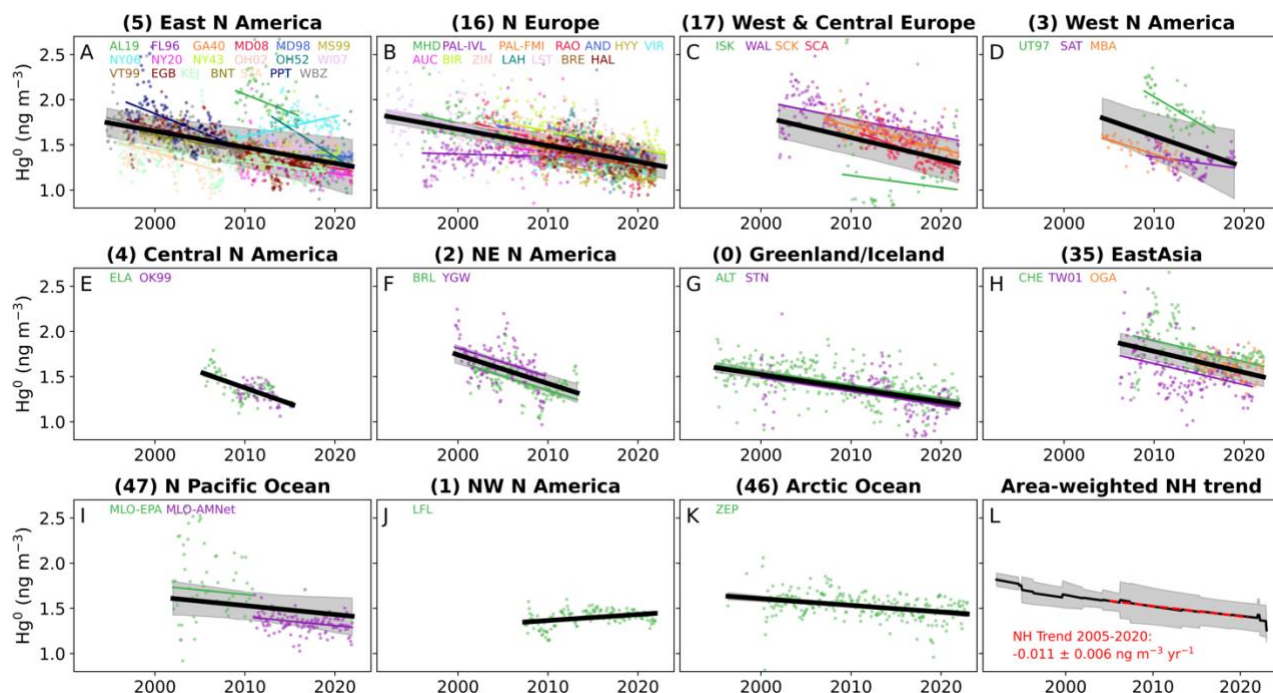
800

801

802 Figures

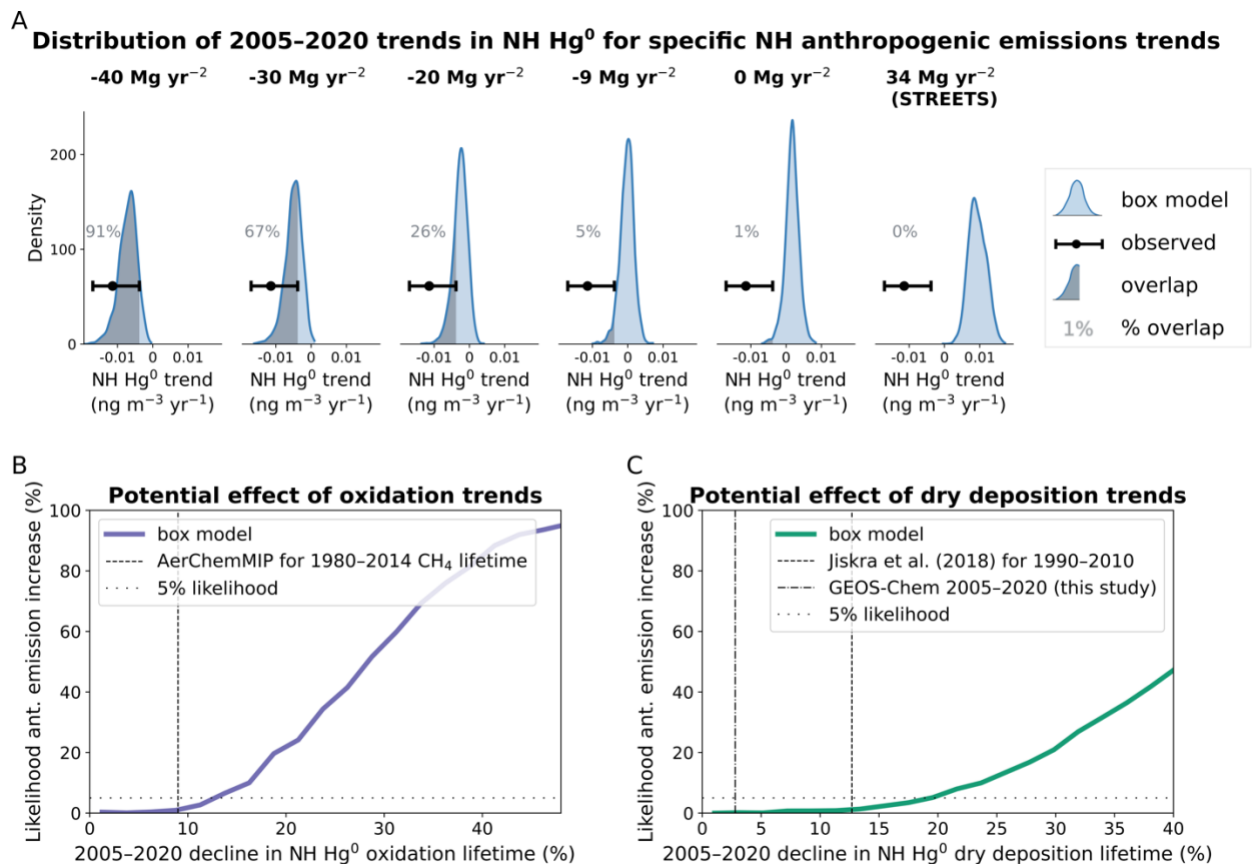


803
 804 **Figure 1.** Map of observation stations that measured atmospheric Hg concentrations for more than 6
 805 years (Table S1). Defined regions (26) are indicated with black lines, with corresponding numbering of
 806 included regions listed on the map. For this study, we included NH stations with openly accessible or
 807 provided datasets.
 808

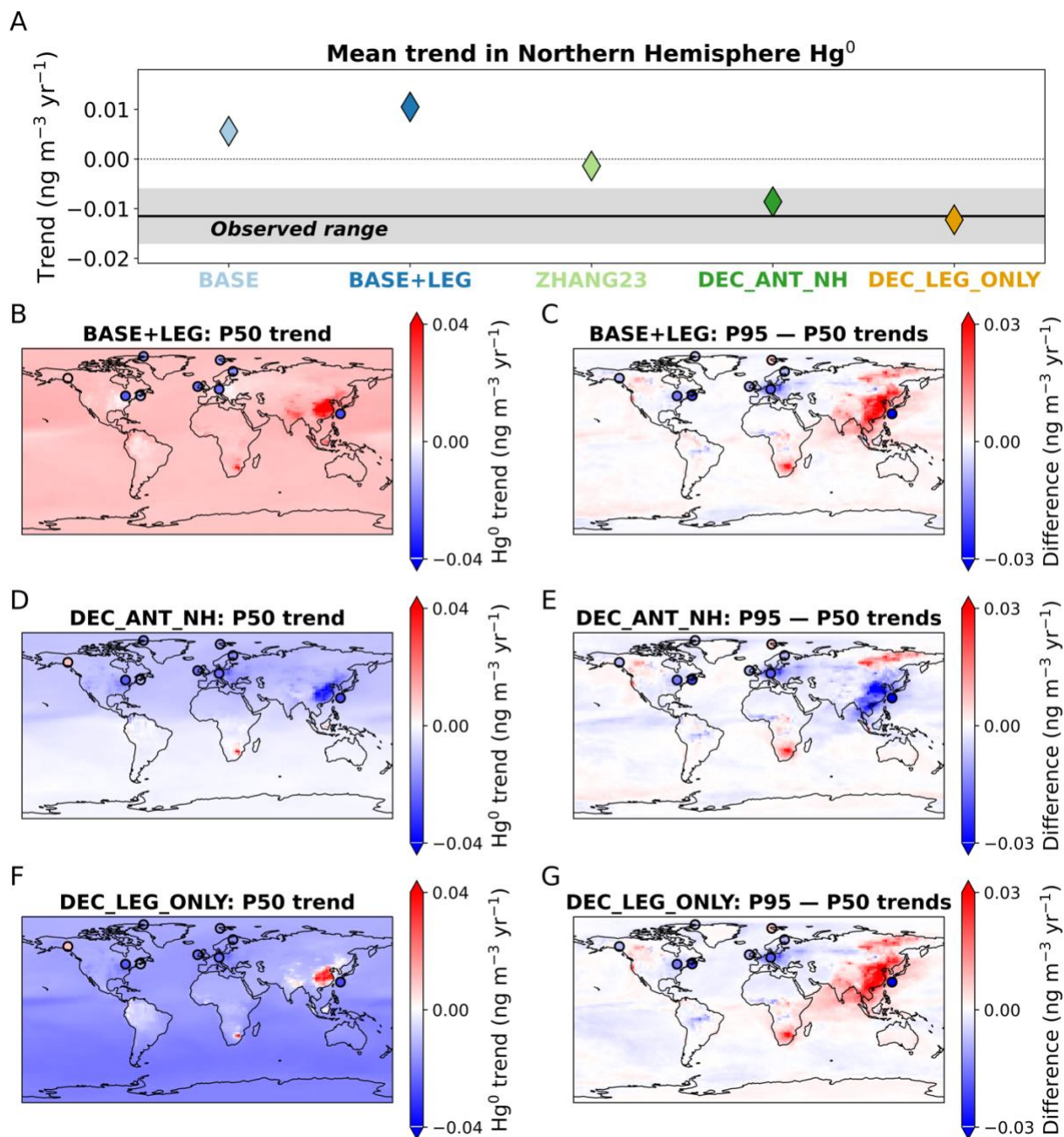


809
 810 **Figure 2.** Trends in observed gaseous elemental mercury (Hg^0) aggregated by the regions (A–K) in Fig. 1
 811 (labelled by region number). Trends are calculated with linear mixed effects modeling, with overall
 812 regional trends shown in black and shading shows the 5th to 95th percentile range. Individual site
 813 deseasonalized monthly means are shown as colored points and individual regressions as colored lines.
 814 The overall Northern Hemisphere (NH) trend (L) is calculated by taking the area-weighted average of
 815 regional trends, with the shading showing the 2σ averaging error. The red dashed curve in L is the linear
 816 regression trend for 2005–2020, with trend error representing 2σ error from resampling regional trends
 817 within their error bounds. We distinguished data from sites where measurements were made by multiple
 818 networks, i.e., Pallas (FMI and IVL) and Mauna Loa (EPA and AMNet).

819
 820



821
 822 **Figure 3.** Modeled relationships between 2005–2020 trends in NH Hg⁰ concentrations and drivers. (A)
 823 Histograms showing relationship between 2005–2020 trends in anthropogenic NH emissions and NH Hg⁰
 824 trends. We select scenarios with different anthropogenic emissions trend values from the 10⁵ box model
 825 simulations (with a window of ± 1 Mg yr⁻² to yield ~ 2000 simulations for each trend value). Blue histograms
 826 illustrate the probability density of simulated NH Hg⁰ trends for each emission trend value. Observed NH
 827 Hg⁰ trends are shown in the horizontal black line with error bars. The shaded overlap represents the area
 828 of the histogram where the model is compatible with observed trends, with the percent of total area
 829 shown in grey. The histogram for the anthropogenic emissions trend of 34 Mg yr⁻² represents the Streets
 830 et al. (10) 2005–2015 trend. (B) Impact of NH Hg⁰ oxidation lifetime trends on the likelihood of positive
 831 anthropogenic (ant.) trends for 2005–2020. The x-axis shows the relative decline (%) in the NH Hg⁰
 832 oxidation lifetime between 2005 and 2020. The y-axis refers to the percent of box model runs fitting with
 833 the observed NH Hg⁰ trend ($\pm 2\sigma$) that have positive anthropogenic emissions trends. The AerChemMIP
 834 (32) estimate for the relative change 1980–2014 methane (CH₄) oxidation lifetime is shown for context. (C)
 835 Impact of NH Hg⁰ dry deposition lifetime on the likelihood of positive anthropogenic (ant.) trends for 2005–
 836 2020. The x-axis shows the relative decline (%) in the NH Hg⁰ dry deposition lifetime between 2005 and
 837 2020. The estimated trend in NH dry deposition from Jiskra et al. (20) for 1990–2010 is shown for context,
 838 as well as the GEOS-Chem simulated 2005–2020 trend (Fig. S11).
 839



840
 841 **Figure 4.** Comparison between trends (2005–2020) in GEOS-Chem model simulations and observations
 842 for Northern Hemisphere (NH) mean Hg^0 (A), calculated using linear mixed effects modeling of available
 843 NH regions and calculating the area-weighted mean (Fig. 2). The observed range in the NH Hg^0 trend is
 844 shown as a black line (mean) with shaded area ($\pm 2\sigma$). Error bars are smaller than the markers for the
 845 model simulations. Trend in median (P50) daily deseasonalized simulated values in BASE+LEG (B),
 846 DEC_ANT_NH (D), and DEC_LEG_ONLY (F) for each model grid cell. BASE+LEG is the simulation with
 847 Streets et al. (10) emissions and associated legacy feedbacks, DEC_ANT_NH is the simulation with
 848 decreasing anthropogenic emissions in the NH, and DEC_LEG_ONLY includes a decline in legacy
 849 emissions from the ocean (Table 1). Observed results are plotted in filled circles for 9 stations with more
 850 than 13 years of high frequency data. Differences between 95th percentile (P95) trend and median (P50)
 851 trend shown for BASE+LEG (C), DEC_ANT_NH (E), and DEC_LEG_ONLY (G) simulations and
 852 observations. The other simulations are shown in Fig. S13.

853 **Table 1.** Description of Hg simulations conducted in GEOS-Chem for 2005–2020.

Simulation	Anthropogenic emissions	Legacy re-emissions	Anthropogenic NH emissions trend (Mg yr⁻²)	Overall NH emissions trend (Mg yr⁻²)
BASE	2005–2015: Streets et al. (10) 2016–2020: repeat 2015	Constant interannually; based on Horowitz et al. (43)	+23	+18
BASE+LEG	2005–2015: Streets et al. (10) 2016–2020: repeat 2015	Trend from median response to BASE anthropogenic emissions trend (Fig. S9F)	+23	+31
ZHANG23	2005–2020 Chinese emissions from BASE are scaled by emission inventory trend from Zhang et al. (45)	Trend from median response to ZHANG23 anthropogenic emissions trend (Fig. S9F)	-11	-12
DEC_ANT_NH	ZHANG23 emissions with additional 23 Mg yr ⁻² decrease in anthropogenic emissions spread across NH outside China	Trend from median response to DEC_ANT_NH anthropogenic emissions trend (Fig. S9F)	-34	-41
DEC_LEG_ONLY	2005–2015: Streets et al. (10) 2016–2020: repeat 2015	Decline imposed	+23	-30

854

1 **Supplementary Information (SI) for**

2 Unexpected anthropogenic emission decreases explain recent atmospheric mercury
3 concentration declines

4

5 Aryeh Feinberg^{a*}, Noelle E. Selin^{a,b}, Christine F. Braban^c, Kai-Lan Chang^{d,e}, Danilo Custódio^f, Daniel A.
6 Jaffe^{g,h}, Katriina Kyllönenⁱ, Matthew S. Landis^j, Sarah R. Leeson^c, Winston Luke^k, Koketso M. Molepo^l,
7 Marijana Murovec^m, Michelle G. Nerentorp Mastromonacoⁿ, Katrine Aspmo Pfaffhuber^o, Julian Rüdiger^p,
8 Guey-Rong Sheu^q, and Vincent L. St.Louis^r

9 ^a *Institute for Data, Systems, and Society, Massachusetts Institute of Technology, Cambridge, MA 02139,*
10 *USA*

11 ^b *Department of Earth, Atmospheric, and Planetary Sciences, Massachusetts Institute of Technology,*
12 *Cambridge, MA 02139, USA*

13 ^c *UK Centre for Ecology & Hydrology (UKCEH), Penicuik, Midlothian EH26 0QB, UK*

14 ^d *Cooperative Institute for Research in Environmental Sciences, University of Colorado, Boulder, CO*
15 *80309-0401, USA*

16 ^e *NOAA Chemical Sciences Laboratory, Boulder, CO 80305, USA*

17 ^f *Max-Planck-Institut für Biogeochemie, D-07745 Jena, Germany*

18 ^g *School of STEM, University of Washington Bothell, Bothell, WA 98011, USA*

19 ^h *Department of Atmospheric Sciences, University of Washington Seattle, Seattle, WA 98195, USA*

20 ⁱ *Finnish Meteorological Institute, Helsinki 00560, Finland*

21 ^j *United States Environmental Protection Agency, Office of Research and Development, Research*
22 *Triangle Park, NC 27711, USA*

23 ^k *NOAA/Air Resources Laboratory, College Park, MD 20740, USA*

24 ^l *Institute of Coastal Environmental Chemistry, Helmholtz Zentrum Hereon, 21502 Geesthacht, Germany*

25 ^m *Slovenian Environment Agency, Environment and Nature protection Office, Air Quality Division, 1000*
26 *Ljubljana, Slovenia*

27 ⁿ *IVL Swedish Environmental Research Institute, SE-411 33 Gothenburg, Sweden*

28 ^o *NILU, 2027 Kjeller, Norway*

29 ^p *Air Monitoring Network, German Environment Agency, 63225 Langen, Germany*

30 ^q *Department of Atmospheric Sciences, National Central University, Taoyuan 320, Taiwan*

31 ^r *Department of Biological Sciences, University of Alberta, Edmonton, AB T6G 2E9, Canada*

32 *Correspondence to: arifeinberg@gmail.com (A.F.)

33 **This PDF file includes:**

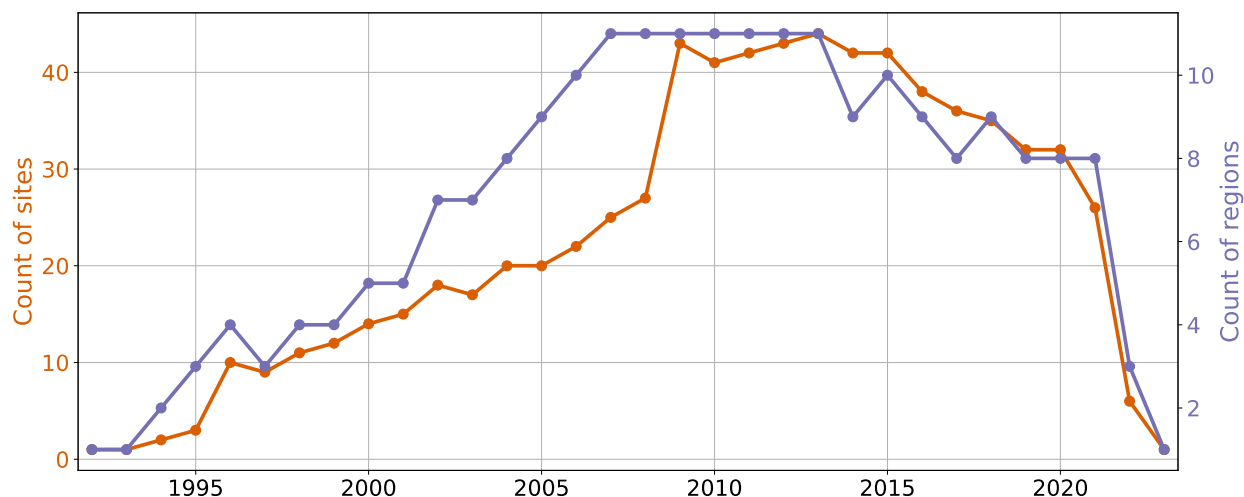
34 Supplementary Text
35 Figures S1 to S15
36 Tables S1 to S4
37 Supplementary References

38 **Section S1. Observation station information**

39 **Table S1.** List of sites measuring gaseous elemental mercury (GEM: Hg⁰) or total gaseous mercury (TGM)
40 included in this study.

Site code	Location	Latitude	Longitude	Measurement network	IPCC region ^a	Years available	Measured quantity
AL19	Birmingham, USA	33.6	-86.8	AMNet ^b	5	2009–2015	Hg ⁰
FL96	Pensacola, USA	30.5	-87.4	AMNet ^b	5	2009–2015	Hg ⁰
GA40	Yorkville, USA	33.9	-85.0	AMNet ^b	5	2009–2015	Hg ⁰
MD08	Piney Reservoir, USA	39.7	-79.0	AMNet ^b	5	2009–2021	Hg ⁰
MD98	Beltsville, USA	39.0	-76.8	AMNet ^b	5	2009–2021	Hg ⁰
MS99	Grand Bay, USA	30.4	-88.4	AMNet ^b	5	2009–2020	Hg ⁰
NY06	Bronx, USA	40.9	-73.9	AMNet ^b	5	2008–2020	Hg ⁰
NY20	Huntington Forest, USA	44.0	-74.2	AMNet ^b	5	2009–2021	Hg ⁰
NY43	Rochester, USA	43.1	-77.5	AMNet ^b	5	2008–2020	Hg ⁰
OH02	Athens, USA	39.3	-82.1	AMNet ^b	5	2009–2020	Hg ⁰
OH52	South Bass Island, USA	41.7	-82.8	AMNet ^b	5	2013–2021	Hg ⁰
OK99	Stilwell, USA	35.8	-94.7	AMNet ^b	4	2009–2015	Hg ⁰
UT97	Salt Lake City, USA	40.7	-112.0	AMNet ^b	3	2008–2017	Hg ⁰
VT99	Underhill, USA	44.5	-72.9	AMNet ^b	5	2009–2016	Hg ⁰
WI07	Horicon Marsh, USA	43.5	-88.6	AMNet ^b	5	2011–2017	Hg ⁰
MLO	Mauna Loa, USA	19.5	-155.6	AMNet ^b /EPA ^c /NOAA	47	2002–2021	Hg ⁰
MBA	Mt. Bachelor, USA	44.0	-121.7	GMOS ^d	3	2004–2012	Hg ⁰ / TGM [*]
ALT	Alert, Canada	82.5	-62.3	ECCC ^e	0	1995–2021	Hg ⁰ / TGM [†]
BNT	Burnt Island, Canada	45.8	-82.9	ECCC ^e	5	1998–2007	TGM
BRL	Bratt's Lake, Canada	50.2	-104.7	ECCC ^e	2	2001–2013	TGM
EGB	Egbert, Canada	44.2	-79.8	ECCC ^e	5	1996–2018	TGM
KEJ	Kejimikujik, Canada	44.4	-65.2	AMNet ^b / ECCC ^e	5	1996–2018	Hg ⁰ / TGM [‡]
LFL	Little Fox Lake, Canada	61.4	-135.6	ECCC ^e	1	2007–2021	TGM
PPT	Point Petre, Canada	43.8	-77.1	ECCC ^e	5	1996–2007	TGM
SAT	Saturna, Canada	48.8	-123.2	ECCC ^e	3	2009–2018	TGM
STA	Huntsman Science Centre, Canada	45.1	-67.1	ECCC ^e	5	1995–2007	TGM
WBZ	St. Anicet, Canada	45.1	-74.3	ECCC ^e	5	1994–2009	TGM
YGW	Kuujuarapik, Canada	55.3	-77.7	ECCC ^e	2	1999–2009	TGM
ELA	Experimental Lakes Area, Canada	49.7	-93.7	IISD ^f	4	2005–2013	Hg ⁰
AND	Andøya, Norway	69.3	16.0	EMEP ^g	16	2004–2021	Hg ⁰
AUC	Auchencorth Moss, UK	55.8	-3.2	EMEP ^g	16	2006–2022	Hg ⁰ / TGM [#]
BIR	Birkenes, Norway	58.4	8.3	EMEP ^g	16	2004–2023	Hg ⁰ / TGM [§]
BRE	Bredkälen, Sweden	63.9	15.3	EMEP ^g	16	2009–2021	TGM
HAL	Hallahus/Vaviihill ^h , Sweden	56.0	13.1	EMEP ^g	16	2009–2021	TGM
HYY	Hyytiälä, Finland	61.6	24.0	EMEP ^g	16	2009–2021	TGM
ISK	Iskrba, Slovenia	45.6	14.9	EMEP ^g	17	2009–2021	TGM
LAH	Lahemaa, Estonia	59.5	25.9	EMEP ^g	16	2012–2021	Hg ⁰
LST	Lista, Norway	58.1	6.6	EMEP ^g	16	1992–2004	TGM
MHD	Mace Head, Ireland	53.3	-9.9	EMEP ^g /GMOS ^d	16	1996–2022	TGM
PAL	Pallas, Finland	68.0	24.4	EMEP ^g /GMOS ^d	16	1996–2021	TGM
RAO	Rådö, Sweden	57.4	11.9	EMEP ^g /GMOS ^d	16	2002–2020	TGM
SCA	Schauinsland, Germany	47.9	7.9	EMEP ^g	17	2011–2021	TGM
SCK	Schmücke, Germany	50.7	10.8	EMEP ^g	17	2007–2021	TGM
STN	Station Nord/Villum, Greenland	81.6	-16.6	EMEP ^g	0	2000–2021	TGM
VIR	Virolahti, Finland	60.5	27.7	EMEP ^g	16	2008–2021	TGM
WAL	Waldhof, Germany	52.8	10.8	EMEP ^g	17	2002–2021	TGM
ZEP	Zeppelin, Norway	78.9	11.9	EMEP ^g	46	1996–2022	Hg ⁰ / TGM [¶]
ZIN	Zingst, Germany	54.4	12.7	EMEP ^g	16	1999–2021	TGM
TW01	Mt. Lulin, Taiwan	23.5	120.9	AMNet ^b / MOENV Taiwan ⁱ	35	2006–2020	Hg ⁰
CHE	Cape Hedo, Japan	26.9	128.3	MOEJ ^j	35	2007–2022	Hg ⁰
OGA	Oga Peninsula, Japan	39.9	139.9	MOEJ ^j	35	2014–2022	Hg ⁰

41 ^a IPCC regions are defined with the numbering in Fig. 1, taken from Iturbide et al. (1) ^b Gay et al. (2) ^c Carbone et al. (3)
42 ^d Sprovieri et al. (4) ^e Cole et al. (5) ^f St. Louis et al. (6) ^g Tørseth et al. (7) ^h Site changed location in 2016, but due to nearby locations
43 (<3 km apart), they are combined in this analysis ⁱ Nguyen et al. (8) ^j Marumoto et al. (9)
44 ^{*} MBA: TGM (2004) and Hg⁰ (2005–2012) [†] ALT: TGM (1995–2021) and Hg⁰ (2002–2021); analyzed TGM
45 [‡] KEJ: TGM (1996–2018) and Hg⁰ (2009–2018); analyzed TGM [#] AUC: TGM (2006–2013) and Hg⁰ (2012–2022)
46 [§] BIR: TGM (2004–2010) and Hg⁰ (2011–2023) [¶] ZEP: TGM (1996–2000) and Hg⁰ (2000–2022)



47
 48 **Figure S1.** Timeseries showing count of measurement sites included in this study by operation year. The
 49 orange curve shows the number of sites measured in each year and the purple curve shows the number
 50 of Northern Hemisphere (NH) IPCC regions (Fig. 1) measured in each year. Note that 2022 and 2023
 51 data may still be undergoing quality control procedures by networks and therefore was not yet released at
 52 the time of analysis; more data from these years will likely be made available in the future.

53
 54 **Section S2. Trend results by region**

56 **Table S2.** Tabulated overall regional trends ($\pm 2\sigma$) calculated through linear mixed effects modelling for
 57 full available time period of each region.

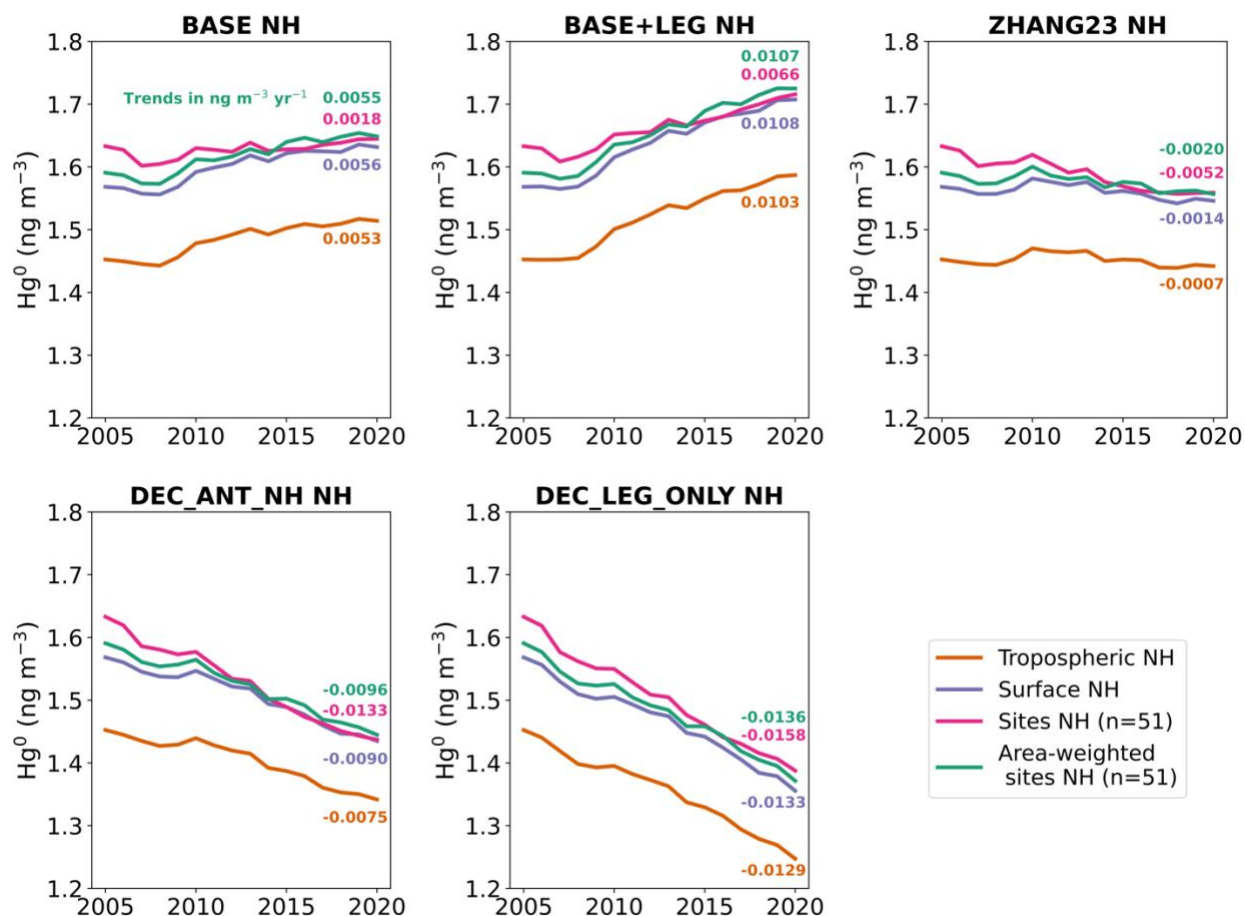
Region name (number)	Number of sites	Area (10^6 km^2)	Trend ($\text{ng m}^{-3} \text{ yr}^{-1}$)	Time period
Eastern North America (5)	19	5.69	-0.016 ± 0.011	1994–2022
Northern Europe (16)	13	5.00	-0.018 ± 0.004	1992–2023
West & Central Europe (17)	4	3.79	-0.024 ± 0.010	2002–2021
Western North America (3)	3	3.14	-0.035 ± 0.025	2004–2018
Central North America (4)	2	2.93	-0.035 ± 0.007	2005–2015
Northeastern North America (2)	2	7.66	-0.032 ± 0.009	1999–2013
Greenland/Iceland (0)	2	4.77	-0.015 ± 0.003	1995–2021
East Asia (35)	3	9.46	-0.023 ± 0.005	2006–2022
North Pacific Ocean (47)	1	51.61	-0.010 ± 0.011	2002–2021
Northwestern North America (1)	1	7.51	0.007 ± 0.003	2007–2021
Arctic Ocean (1)	1	6.35	-0.007 ± 0.002	1996–2022
Northern Hemisphere (NH) area-weighted average	51		-0.011 ± 0.006	2005–2020

58
 59

60 Section S3. Sensitivity of trends to statistical approach**61 Section S3.1 Modelled differences between site, surface, and troposphere NH trends**

62 We used the five GEOS-Chem simulations to test different approaches for calculating overall trends in NH
63 Hg^0 (Fig. S2). We calculated annual averages of the model results over the entire NH troposphere
64 (orange lines), representative of the NH tropospheric box in the 3-box model simulations. We compared
65 this to simulated NH surface Hg^0 concentrations (purple lines), which is the quantity that can actually be
66 measured by surface observation stations. The calculated 2005–2020 trends in surface Hg^0 agree within
67 $0.0007 \text{ ng m}^{-3} \text{ yr}^{-1}$ of tropospheric Hg^0 trends for all simulations except DEC_ANT_NH, where surface
68 declines are faster than tropospheric declines by $0.0015 \text{ ng m}^{-3} \text{ yr}^{-1}$. This can be explained by enhanced
69 dilution of the negative emissions trends when considering the whole troposphere versus the surface
70 level. To approximate the real situation where only a small fraction of the NH surface is measured, we
71 averaged only the model grid cells that contain the 51 observation sites (magenta line in Fig. S2). This
72 approach leads to biases of up to $0.0044 \text{ ng m}^{-3} \text{ yr}^{-1}$ due to the uneven distribution of observation stations
73 (Fig. 1) throughout the NH, with some regions covered more than others and other regions having no
74 observations. This bias can be reduced to below $0.0006 \text{ ng m}^{-3} \text{ yr}^{-1}$ by first averaging by IPCC region the
75 grid cells that correspond to observation sites (Fig. 1) and then calculating an area-weighted average for
76 the NH (green line), similar to what was done for the observation analysis in the main manuscript (Fig. 2).
77 Therefore, it is best to use the approach of area-weighted site averages when limited observation stations
78 are available, leading to good agreement with the surface trends in Hg^0 . We expanded the observed trend
79 uncertainty in Figs. 3A and B upwards by $0.0021 \text{ ng m}^{-3} \text{ yr}^{-1}$ (max error between area-weighted and
80 tropospheric trends, DEC_ANT_NH), due to the potential overestimate of NH tropospheric trends by only
81 having surface observations (Fig. S2).

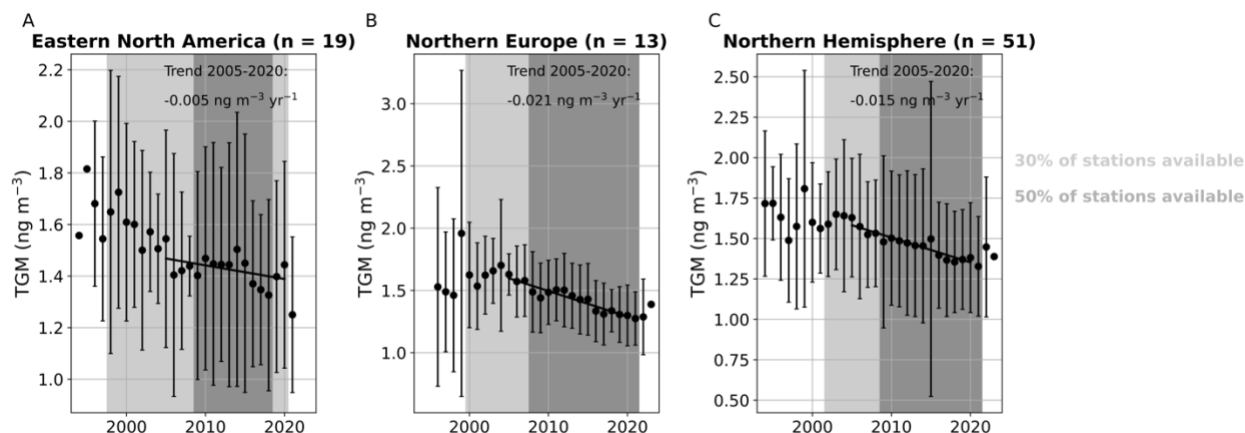
82



83
 84 **Figure S2.** Different methods of calculating hemispheric average trends applied to GEOS-Chem
 85 simulated Hg⁰. We compared annual mean simulated timeseries of: 1) NH tropospheric averages, 2) NH
 86 surface averages, 3) averaging model grid cells where observation sites are located, and 4) area-
 87 weighted averaging of regional averages of model grid cells where observation sites are located. Linear
 88 regression trends over 2005–2020 are listed in units of ng m⁻³ yr⁻¹.

89
 90 *Section S3.2 Aggregation of observation stations into overall NH annual averages using “bucket” method*
 91 Previous studies (e.g., 10) have calculated overall timeseries for regions by averaging all available
 92 stations for each specific year (“bucket” method). Biases can arise in this approach from multiple sources
 93 of error: 1) sites have individual offsets and trends due to measurement method differences or specific
 94 local sources, leading to biases in a “bucket” average because sites do not all cover the same time
 95 period; 2) sites are unevenly distributed, with certain regions over- or under-represented; and 3) certain
 96 months can be missing in a specific year, which due to the strong seasonality of Hg⁰ can bias the annual
 97 mean. We aimed to address the drawbacks of the “bucket” approach by explicitly modeling offsets
 98 between sites using linear mixed effects models, deseasonalizing monthly means from all observations,
 99 and aggregating results by IPCC regions before calculating area-weighted averages. To compare our
 100 methods with approaches applied in previous papers, we use the bucket approach to calculate 2005–
 101 2020 trends in Eastern North America (19 sites), Northern Europe (13 sites), and the NH (51 sites) (Fig.
 102 S3) in a sensitivity test. Overall, the derived trends are similar for the NH between our approach (-0.011 ±
 103 0.006 ng m⁻³ yr⁻¹) and the “bucket” approach (-0.015 ng m⁻³ yr⁻¹). Issues with the bucket method were
 104 observed for periods when less sites are available (e.g., before the year 2000 in Fig. S3), which show
 105 high variability due to differences in the number and characteristics of averaged sites for each year.

106 Therefore, we recommend that caution be exercised with such an approach, as the derived aggregated
 107 timeseries may be misleading and could be misinterpreted as real variability rather than changes in site
 108 availability.
 109



110
 111 **Figure S3.** “Bucket” method trends calculated by averaging all available station data (not
 112 deseasonalized) for each year for Eastern North America (A), Northern Europe (B), and the overall
 113 Northern Hemisphere (C). Error bars show the 2σ variation in station averages. Shading shows the years
 114 where at least 30% (light gray) and 50% of the stations (dark gray) are available. Linear regression trends
 115 are calculated over 2005–2020 and listed on the plot.
 116

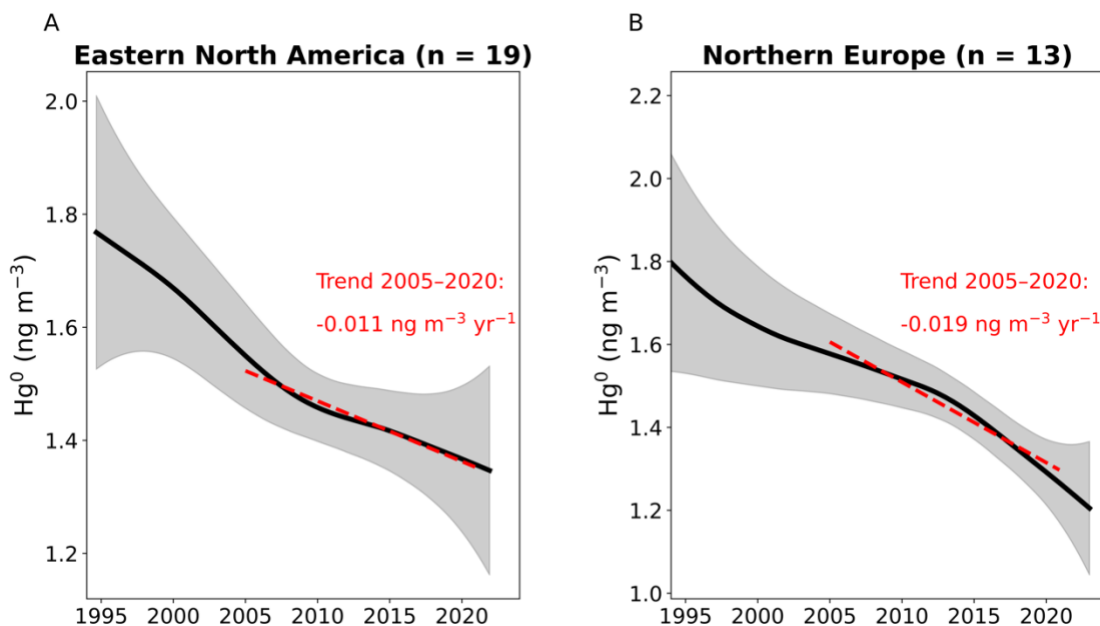
117 *Section S3.3 Using Generalized Additive Models (GAM) to aggregate multisite data*

118 To test the robustness of our regional trend results to other approaches, we applied the approach of
 119 Chang et al. (11) to use Generalized Additive Models (GAM) to aggregate multisite data into an overall
 120 trend. In this regression-based approach, we modeled the deseasonalized Hg^0 monthly mean values at
 121 multiple sites as a function of site (s) and time (t):
 122

$$\text{obs}(s,t) = \text{regional trend}(t) + \text{regional seasonality}(t) + \text{site offset}(s) + \text{site-specific trend}(s,t) + \text{site-specific seasonality}(s,t) + \text{AR}(1) \text{ error} \quad (\text{Eq. S1})$$

123
 124
 125
 126
 127 The GAM approach fits smooth functions of the predictor variables, which include time, month-of-year (for
 128 seasonality), and the categorical site ID (for site-specific terms). We used the implementation of GAM in
 129 the R package mgcv (12) and calculated fits using the restricted maximum likelihood (REML) method to
 130 avoid overfitting.
 131

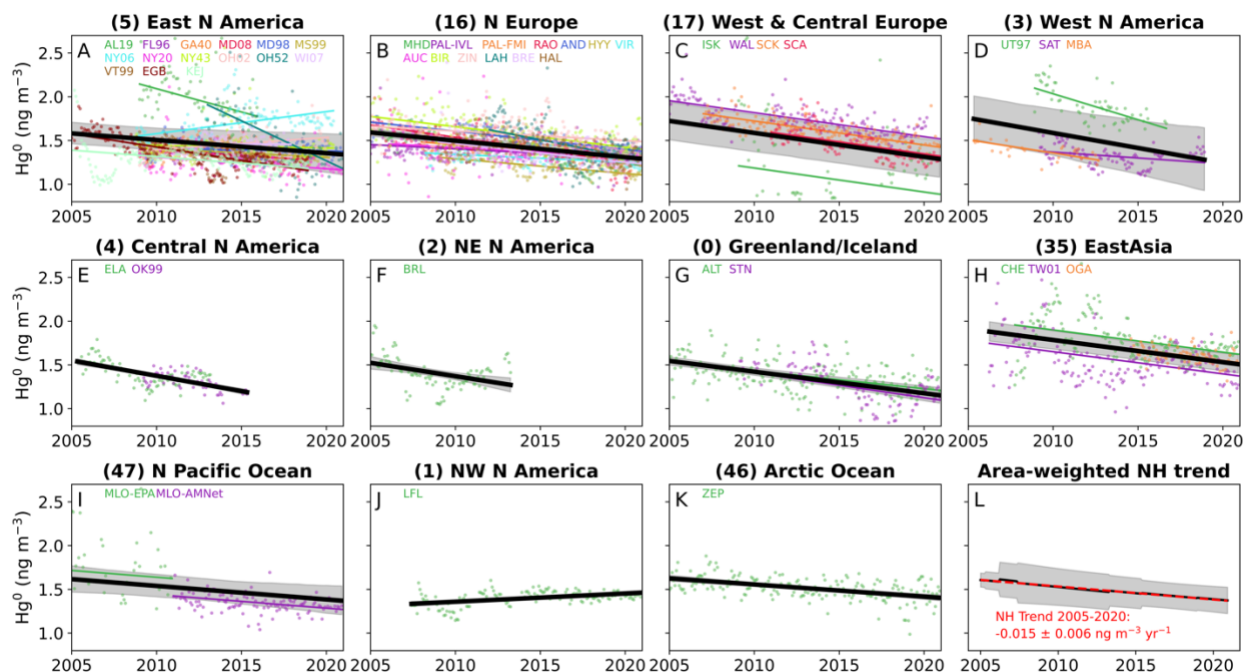
132 The GAM method is not suitable when only a few sites are available within a region (13), so in the main
 133 manuscript we focused on linear mixed effect models of regional trends. For the GAM analysis here, we
 134 investigated the two regions with more than 10 sites (Eastern North America and Northern Europe). GAM
 135 helped to identify nonlinearities in the overall regional trend, for example, a deceleration in the Eastern
 136 North America Hg^0 decline occurred after ~ 2009 . A previous study has suggested a deceleration in Hg^0
 137 trends in North America around 2008, although different statistical methods were applied on a smaller set
 138 of stations (14). We calculated the 2005–2020 linear trend obtained from the GAM curves for Eastern
 139 North America ($-0.011 \text{ ng m}^{-3} \text{ yr}^{-1}$) and Northern Europe ($-0.019 \text{ ng m}^{-3} \text{ yr}^{-1}$). Since both of these trends
 140 are within the error of the results obtained for linear mixed effects modeling (Eastern North America: $-$
 141 $0.016 \pm 0.011 \text{ ng m}^{-3} \text{ yr}^{-1}$; Northern Europe: $-0.018 \pm 0.004 \text{ ng m}^{-3} \text{ yr}^{-1}$), we conclude that the derived
 142 regional declines are relatively robust to the choice of statistical approach.



143
 144 **Figure S4.** Generalized additive model (GAM) regional trends for multisite deseasonalized total gaseous
 145 mercury (Hg^0) data in Eastern North America (A) and Northern Europe (B). The GAM mean estimate is
 146 shown as a black line, with shaded grey areas showing ± 2 standard errors in the GAM estimate. Linear
 147 regression trends (red dashed lines) were calculated over the 2005–2020 period from the regional
 148 nonlinear GAM curve.

149
 150 *Section S3.4 Restricting the analysis to site data between 2005 and 2020*

151 In the main manuscript (Fig. 2), we use the full set of available data between 1992 and 2022 to calculate
 152 linear mixed effects model trends for each region, which are then area-weighted to calculate an average
 153 2005–2020 trend for the Northern Hemisphere (NH). We use the full extent of data to maximize the
 154 available information in the calculation of long-term Hg^0 trends. Here, we repeat the analysis but only use
 155 data between 2005 and 2020 to calculate the trend, removing all earlier and later data from the analysis.
 156 The results are summarized in Fig. S5 and Table S3, which can be compared to Fig. 2 and Table S2.
 157 Overall, the regional trends calculated with both datasets are overlapping in their error ranges, with the
 158 exception of the Arctic Ocean region (2005–2020: $-0.014 \pm 0.004 \text{ ng m}^{-3} \text{ yr}^{-1}$; 1996–2022: -0.007 ± 0.002
 159 $\text{ng m}^{-3} \text{ yr}^{-1}$). The area-weighted NH average trend in the 2005–2020 calculation is $-0.015 \pm 0.006 \text{ ng m}^{-3}$
 160 yr^{-1} , slightly more negative but overlapping with the trend calculated in the main paper ($-0.011 \pm 0.006 \text{ ng}$
 161 $\text{m}^{-3} \text{ yr}^{-1}$). Overall, our conclusions remain the same that the NH Hg^0 concentrations are declining between
 162 2005 and 2020 and would be difficult to reconcile with increasing NH anthropogenic emissions.



163
 164 **Figure S5.** Similar to Fig. 2 but only for the period of 2005–2020, trends in observed gaseous elemental
 165 mercury (Hg^0) aggregated by the regions (A–K) in Fig. 1 (labelled by region number). Trends are
 166 calculated with linear mixed effects modeling, with overall regional trends shown in black and shading
 167 shows the 5th to 95th percentile range. Individual site deseasonalized monthly means are shown as
 168 colored points and individual regressions as colored lines. The overall Northern Hemisphere (NH) trend
 169 (L) is calculated by taking the area-weighted average of regional trends, with the shading showing the 2 σ
 170 averaging error. The red dashed curve in L is the linear regression trend for 2005–2020, with trend error
 171 representing 2 σ error from resampling regional trends within their error bounds.

172
 173

174 **Table S3.** Tabulated overall regional trends ($\pm 2\sigma$) calculated through linear mixed effects modelling after
 175 restricting site data to 2005–2020 period only. See Table S2 for trends calculated using all data.

Region name (number)	Number of sites	Area (10^6 km^2)	Trend ($\text{ng m}^{-3} \text{ yr}^{-1}$)	Time period
Eastern North America (5)	15	5.69	-0.015 ± 0.015	2005–2020
Northern Europe (16)	12	5.00	-0.019 ± 0.006	2005–2020
West & Central Europe (17)	4	3.79	-0.027 ± 0.005	2005–2020
Western North America (3)	3	3.14	-0.034 ± 0.025	2005–2018
Central North America (4)	2	2.93	-0.035 ± 0.007	2005–2015
Northeastern North America (2)	1	7.66	-0.031 ± 0.016	2005–2013
Greenland/Iceland (0)	2	4.77	-0.025 ± 0.008	2005–2020
East Asia (35)	3	9.46	-0.025 ± 0.006	2006–2020
North Pacific Ocean (47)	1	51.61	-0.015 ± 0.011	2005–2020
Northwestern North America (1)	1	7.51	0.009 ± 0.003	2007–2020
Arctic Ocean (1)	1	6.35	-0.014 ± 0.004	2005–2020
Northern Hemisphere (NH) area-weighted average	45		-0.015 ± 0.006	2005–2020

176

177 **Section S4. Differences between Hg^0 and TGM measurements**

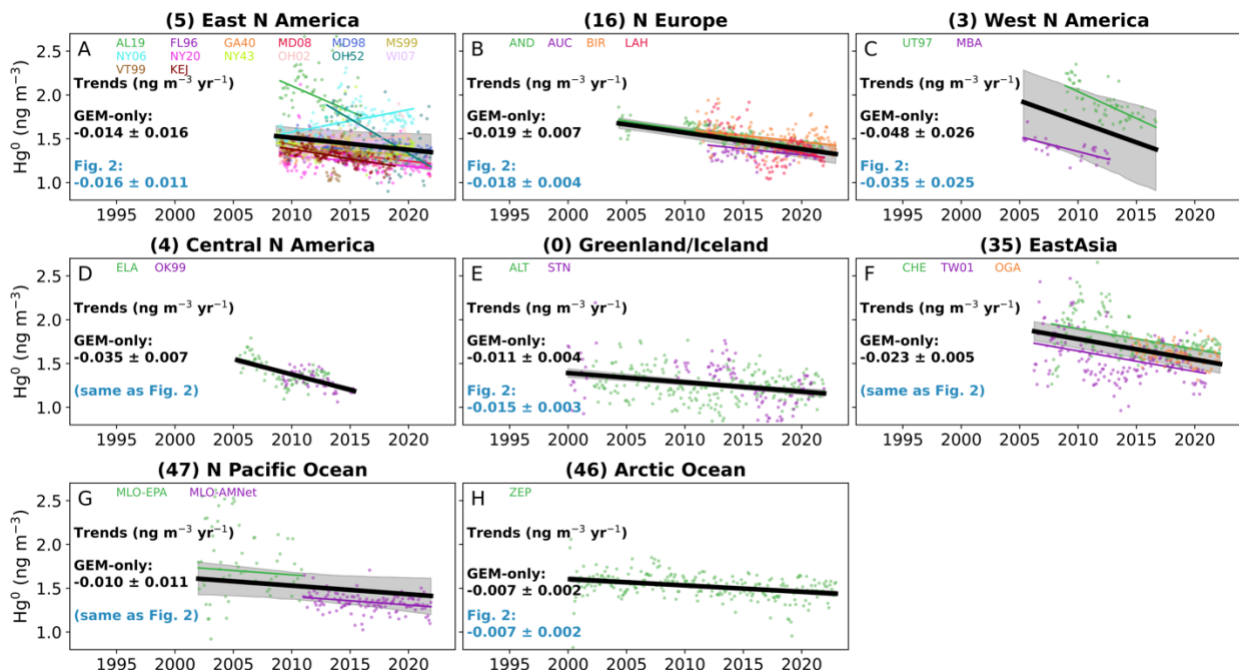
178 Atmospheric Hg is measured in three operationally-defined fractions: gaseous elemental mercury (GEM,
 179 Hg^0), gaseous oxidized mercury (GOM, Hg^{II}), and particulate-bound mercury (PBM, Hg^{P}). Total gaseous
 180 mercury (TGM) refers to the sum of Hg^0 and GOM. Past studies have identified several issues related to
 181 the collection of GOM in Tekran instruments, which leads to a low bias of these measurements that can
 182 vary over space and time (15–17). For this reason, we do not analyze GOM measurements and focus our
 183 analysis on Hg^0 . Previous trend analyses have combined measurements of Hg^0 and TGM, assuming that
 184 Hg^0 is the dominant (>98%) fraction of TGM (10, 18, 19). This is supported by analytical studies showing
 185 that available TGM measurements from networks do not pick up all GOM, and thus represent a fraction
 186 between Hg^0 and true TGM (20). Several measurement networks have also suggested that reported TGM
 187 measurements largely represent Hg^0 concentrations (Environment and Climate Change Canada
 188 [measurement description](#); GMOS: Sprovieri et al. (4)). Therefore, in the main manuscript, we assume that
 189 available TGM and Hg^0 measurements are synonymous and use a combined dataset of these two
 190 quantities.

191

192 To test this assumption, we conducted a sensitivity test analyzing trends from only sites where Hg^0 data
 193 was reported from Tekran or Lumex instruments, removing all TGM data from the analysis. For sites
 194 where both Hg^0 and TGM data are available (Table S1), we analyzed only the Hg^0 data for this sensitivity
 195 test. The results of this sensitivity test analyzing only Hg^0 are shown in Fig. S6, analogous to Fig. 2 in the
 196 main manuscript using the full TGM & Hg^0 dataset. For all regions where TGM measurements were
 197 removed, the trend estimates resulting from using only Hg^0 data overlap with our main manuscript
 198 analysis. No clear patterns are observed in the differences between the GEM-only and all data trends,

199 meaning that any differences are probably driven by differences in the data availability and studied time
 200 period. The trend estimates are:

201
 202 East North America (Fig. S6A) – GEM-only: -0.014 ± 0.016 ng m⁻³ yr⁻¹, all data: -0.016 ± 0.011 ng m⁻³ yr⁻¹
 203 Northern Europe (Fig. S6B) – GEM-only: -0.019 ± 0.007 ng m⁻³ yr⁻¹, all data: -0.018 ± 0.004 ng m⁻³ yr⁻¹
 204 West North America (Fig. S6C) – GEM-only: -0.048 ± 0.026 ng m⁻³ yr⁻¹, all data: -0.035 ± 0.025 ng m⁻³ yr⁻¹
 205 Greenland/Iceland (Fig. S6E) – GEM-only: -0.011 ± 0.004 ng m⁻³ yr⁻¹, all data: -0.015 ± 0.003 ng m⁻³ yr⁻¹
 206 Arctic Ocean (Fig. S6H) – GEM-only: -0.007 ± 0.002 ng m⁻³ yr⁻¹, all data: -0.007 ± 0.002 ng m⁻³ yr⁻¹
 207
 208



209
 210 **Figure S6.** Similar to Fig. 2 but showing only data from Hg⁰ measurements (removing all TGM
 211 measurements from the dataset). Trends in observed gaseous elemental mercury (GEM: Hg⁰) are
 212 aggregated by the regions (A–H) in Fig. 1 (labelled by region number). Trends are calculated with linear
 213 mixed effects modeling, with overall regional trends shown in black and shading shows the 5th to 95th
 214 percentile range. Listed in black are determined regional trend values from the GEM-only analysis with 2σ
 215 errors, while in blue are the trends from the full analysis, including TGM measurements. Three regions
 216 only have GEM data and are thus identical to Fig. 2: Central North America, East Asia, and North Pacific
 217 Ocean. Due to removal of TGM stations, no data is available from the regions: West & Central Europe,
 218 Northeastern North America, and Northwestern North America.

219
 220 All other regions either do not have any sites with Hg⁰ measurements (and thus cannot be evaluated), or
 221 have no sites with TGM measurements (and thus are unchanged from the main manuscript analysis).
 222 Given the overlapping trend estimates between these two analyses, we conclude that the use of both
 223 TGM and Hg⁰ data does not impact the estimates of the overall regional trends. As well, all trend
 224 estimates using only Hg⁰ data also show negative trends and thus support the conclusions in the main
 225 manuscript.

226
 227 Our assumption (applied by previous Hg trend studies as well) that TGM and Hg⁰ measurements can be
 228 combined is supported by this sensitivity test where TGM is fully removed from the trend analysis. We

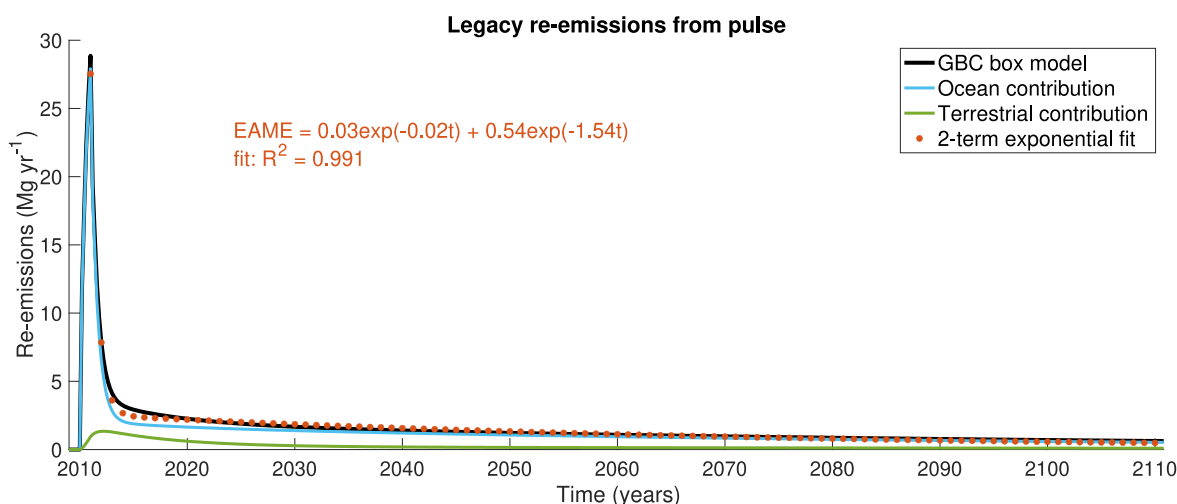
229 therefore chose to keep the analysis using both TGM and Hg⁰ data in the main manuscript as more
 230 locations and time periods are covered.

231
 232 **Section S5. Calculating EAME equations from the GBC box model and perturbation analysis**

233 We followed the approach of Selin (21) to calculate parameters from the EAME equation (Eq. 2) using
 234 pulse simulations in the Hg Global Biogeochemical Box model (GBC) (22, 23). We introduced an
 235 atmospheric Hg pulse of 100 Mg in the year 2010 and monitored the evolution of legacy re-emissions for
 236 100 years, until 2110 (Fig. S7). The two-term exponential model fits the behaviour of the box model very
 237 well ($R^2 \sim 0.99$) on the 100-year time period of the simulation. This fitting reduces the ~ 40 parameters of
 238 the GBC model to 4 understandable parameters, as well as reducing the computation time for legacy re-
 239 emissions. We performed a similar experiment by modeling the release of a riverine pulse, and evaluated
 240 changes to legacy re-emissions. This equation will differ from the atmospheric pulse, as different
 241 timescales are involved (river transport *versus* deposition to oceans) and only a fraction of the riverine
 242 pulse will reach the open ocean and not be buried on the coastal shelf.

243
 244 To estimate a reasonable range in the legacy re-emission pulse parameters (Eq. 2), we performed 1000
 245 parameter perturbation simulations in the GBC model. The 40 relevant parameters that we varied are 35
 246 rate coefficients, 3 parameters for the designation of deposition into soil pools, 1 parameter for geogenic
 247 emissions, and 1 parameter for the fraction of riverine particulate Hg reaching the open ocean. These
 248 parameters were perturbed simultaneously by factors varying between 0.5 and 2, with Latin Hypercube
 249 sampling (24) used to ensure that the parameter space is better explored. For each of the 1000
 250 experiments, we calculated the legacy re-emission pulse parameters (Eq. 2) and selected the 5th–95th
 251 percentile of each parameter as the range for simulations in the 3-box atmospheric model (Table S4). The
 252 1000 experiments were conducted twice, once for atmospheric pulses and once for riverine pulses. The
 253 code for conducting sensitivity experiments in the GBC model is available here:

254 <https://github.com/arifein/gbc-boxmodel-sensitivity>.



255
 256 **Figure S7.** Example of fitting the GBC model pulse experiment to Eq. 2. The contribution of ocean and
 257 terrestrial legacy re-emissions to the total are shown as blue and green lines.

258
 259
 260 **Section S6. 3-box atmospheric model parameter variations**

261 The bounds for the 19 parameters that were varied in the 2×10^5 simulations, along with their
 262 justifications, are listed in Table S4. We sampled the fraction of Hg emitted in the short timescale (f_{short})
 263 and the total re-emissions (E_{total}) instead of directly sampling coefficients a_1 and a_2 in Eq. 2. This is less

264 likely to lead to unrealistic combinations of the a coefficients and the b lifetimes. Integrating Eq. 2
 265 between time 0 and infinity yields an equation for E_{total} :

266
 267
$$E_{\text{total}} = a_1 b_1 + a_2 b_2 \quad (\text{Eq. S2})$$

268
 269 The fraction of Hg emitted in the short timescale is equal to:
 270

271
$$f_{\text{short}} = \frac{a_1 b_1}{a_1 b_1 + a_2 b_2} = \frac{a_1 b_1}{E_{\text{total}}} \quad (\text{Eq. S3})$$

272
 273 We calculated the a coefficients from the sampled variables (b_1 , b_2 , f_{short} , E_{total}) using Eq. S4 and Eq. S5:
 274

275
$$a_1 = \frac{E_{\text{total}} f_{\text{short}}}{b_1} \quad (\text{Eq. S4})$$

276
$$a_2 = \frac{E_{\text{total}} (1 - f_{\text{short}})}{b_2} \quad (\text{Eq. S5})$$

277
 278

279 **Table S4.** Bounds of parameters varied for the 2005–2020 simulations in the 3-box atmospheric model.

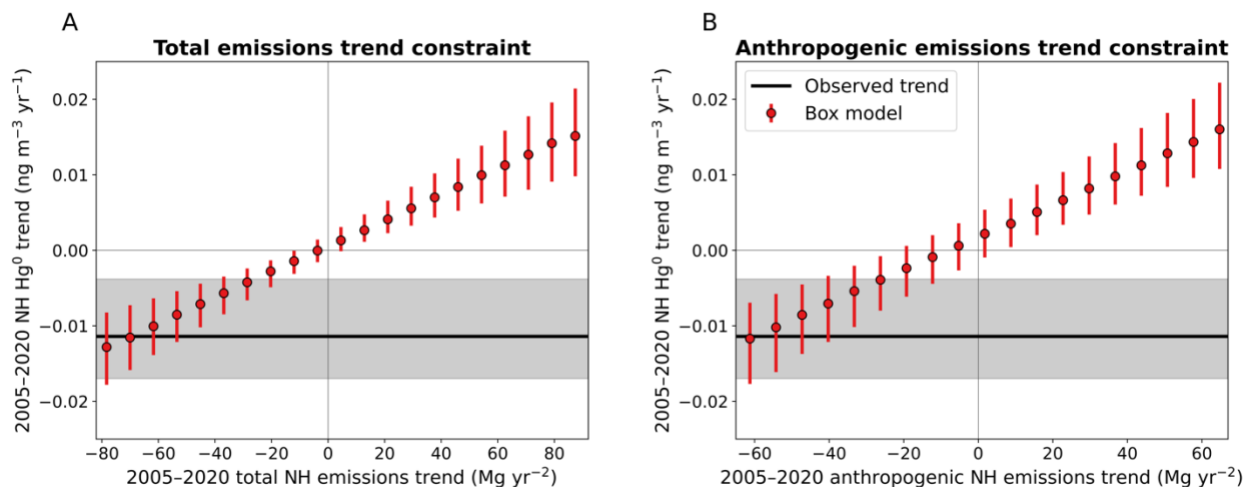
Parameter	Min	Max	Units	Comment/References
Atmospheric Hg lifetime	3	8	months	Horowitz et al. (25); Parrella et al. (26); Zhang et al. (27)
Error in 1970 emissions and releases	-20	+40	%	Error range suggested for 2000, 2010, 2015 emissions in Streets et al. (28)
Error in 1980 emissions and releases	-20	+40	%	Error range suggested for 2000, 2010, 2015 emissions in Streets et al. (28)
Error in 1990 emissions and releases	-20	+40	%	Error range suggested for 2000, 2010, 2015 emissions in Streets et al. (28)
Error in 2000 emissions and releases	-20	+40	%	Error range suggested for 2000, 2010, 2015 emissions in Streets et al. (28)
Error in 2010 emissions and releases	-20	+40	%	Error range suggested for 2000, 2010, 2015 emissions in Streets et al. (28)
Legacy short lifetime (b_1) (atmospheric pulse)	5.7	14.6	months	Based on perturbation analysis of Amos et al. (22, 23) GBC model (Section S5)
Legacy long lifetime (b_2) (atmospheric pulse)	28.6	96.9	years	Based on perturbation analysis of Amos et al. (22, 23) GBC model (Section S5)
Legacy fraction emitted in short timescale (atmospheric pulse)	7	31	%	Based on perturbation analysis of Amos et al. (22, 23) GBC model (Section S5)
Total re-emissions from initial pulse (atmospheric pulse)	79	379	%	Based on perturbation analysis of Amos et al. (22, 23) GBC model (Section S5)
Legacy short lifetime (b_1) (riverine pulse)	1.6	9.5	months	Based on perturbation analysis of Amos et al. (22, 23) GBC model (Section S5)
Legacy long lifetime (b_2) (riverine pulse)	1	116.9	years	Based on perturbation analysis of Amos et al. (22, 23) GBC model (Section S5)
Legacy fraction emitted in short timescale (riverine pulse)	5	55	%	Based on perturbation analysis of Amos et al. (22, 23) GBC model (Section S5)
Total re-emissions from initial pulse (riverine pulse)	2	160	%	Based on perturbation analysis of Amos et al. (22, 23) GBC model (Section S5)
Difference in percent Hg ⁰ emitted from anthropogenic sources between 2020 and 2005	-20	20	%	The speciation of emissions in longest available inventory (29) varied by 15% (from 60% Hg ⁰ in 1970 to 75% Hg ⁰ in 2010)
Anthropogenic emissions trend in Northern Hemisphere (NH)	-70	70	Mg yr ⁻²	Covers wide range without 2020 emissions becoming negative
Anthropogenic emissions trend in Southern Hemisphere (SH)	-10	10	Mg yr ⁻²	Covers wide range without 2020 emissions becoming negative
Deviation of releases trend from emissions trend in NH	-80	80	Mg yr ⁻²	For example, if NH emissions trend is 30 Mg yr ⁻² , the NH releases trend ranges between -21 and 139 Mg yr ⁻² *
Deviation of releases trend from emissions trend in SH	-35	35	Mg yr ⁻²	For example, if SH emissions trend is -10 Mg yr ⁻² , the SH releases trend ranges between -45 and 25 Mg yr ⁻² †

280 * In the NH, decadal release trends in Streets et al. (30) are $1.97 \times$ emissions trends ± 80

281 † In the SH, decadal release trends in Streets et al. (30) are $1.03 \times$ emissions trends ± 35

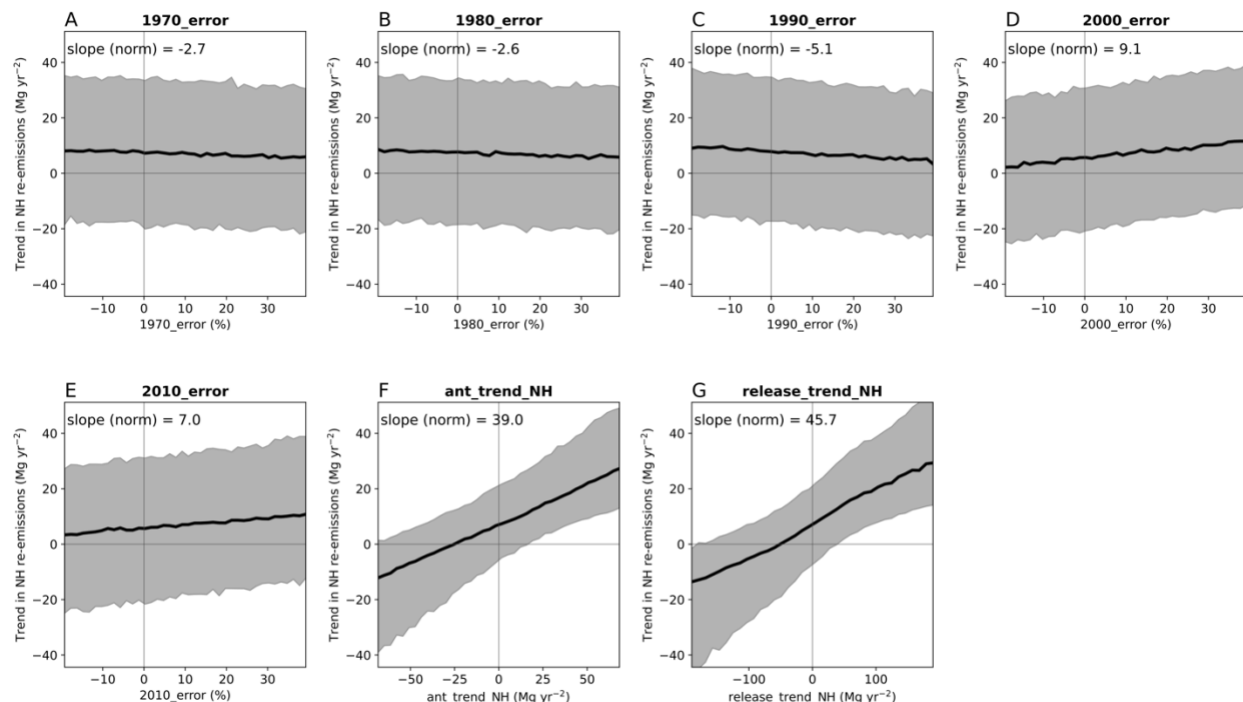
282

283 Fig. S8 visualizes the results of the box model simulations by comparing inputted trends in NH emissions
 284 with simulated trends in NH Hg^0 over 2005–2020. Fig. S8A displays the relationship between total NH
 285 emissions trends (anthropogenic + legacy) and the Hg^0 trend. The NH total emissions trends that would
 286 be compatible with the observed Hg^0 trends (grey range in Fig. S8A) ranges from -15 Mg yr^{-2} to more than
 287 -80 Mg yr^{-2} . The relationship between the total emissions trends and the Hg^0 trend crosses close to the
 288 origin, meaning that with a zero total emissions trend the simulated median Hg^0 trend is negligible.
 289 However, in the case of the anthropogenic emissions trend plot (Fig. S8B), a zero trend in NH
 290 anthropogenic emissions will still lead to a positive Hg^0 trend due to increasing legacy emissions (31).
 291 The NH anthropogenic emissions trend must be below -8 Mg yr^{-2} in order for the NH Hg^0 trend to be
 292 negative. Another aspect of Fig. S8 is that relationship between NH Hg^0 trends and anthropogenic
 293 emissions trends is associated with larger uncertainties (Fig. S8B) than that of total emissions (Fig. S8A),
 294 as evidenced by the larger red error bars in Fig. S8B. The relationship between total NH emissions trends
 295 and the NH Hg^0 concentration trend (Fig. S8A) is mainly affected by uncertainties in the atmospheric Hg
 296 lifetime, SH emissions, and speciation trends. However, the relationship of anthropogenic NH emissions
 297 with Hg^0 concentrations is affected by the uncertain response of legacy emissions to anthropogenic inputs
 298 and the trends in releases to water and land that would accompany anthropogenic emissions trends for
 299 2005–2020, leading to larger error bars.
 300



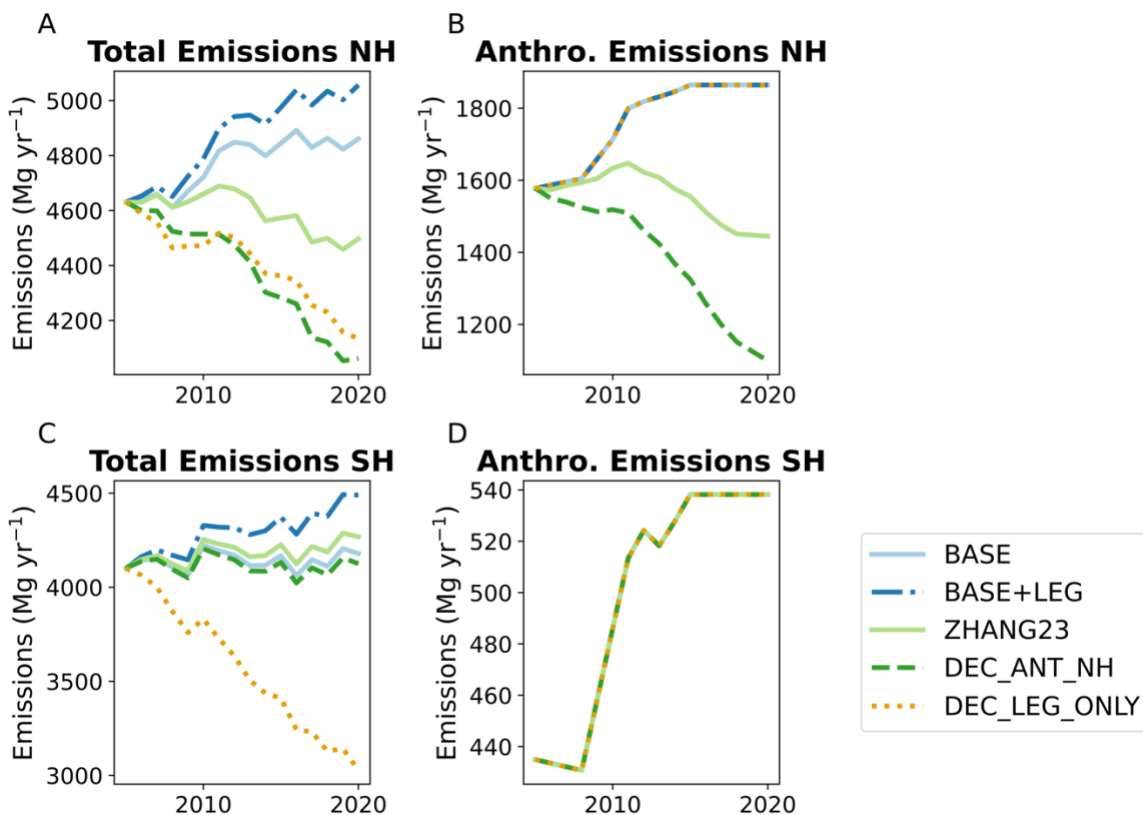
301 **Figure S8.** (A) Relationship between NH Hg^0 trends and the trends in total NH emissions. The 10^5 box
 302 model simulations are summarized in the red points (median) and error bars (5th to 95th percentile).
 303 Observed NH TGM trends are shown in the horizontal black line, with the associated error shaded. The
 304 overlap between grey shading and red error bars represents the parameter space where the model is
 305 compatible with observed trends. (B) Relationship between NH Hg^0 trends and trends in anthropogenic
 306 NH emissions. Fig. 3A in the main manuscript represents a 1-D representation of these curves for
 307 selected values of the anthropogenic NH emissions trend.
 308
 309

310 The relationships between NH Hg re-emissions trends (2005–2020) and anthropogenic emissions and
 311 releases parameters in the 3-box model results are plotted in Fig. S9. We have used Fig. S9F in the main
 312 paper to relate the trend in NH anthropogenic emissions from the GEOS-Chem scenarios with the
 313 expected NH trend in legacy re-emissions. This relationship was used to identify potential trends in legacy
 314 emissions resulting from anthropogenic emissions trends, which can then be incorporated in the GEOS-
 315 Chem simulations by scaling ocean Hg⁰ concentrations.
 316



317
 318 **Figure S9.** The relationships between Northern Hemisphere (NH) Hg re-emissions trends (2005–2020)
 319 and anthropogenic emissions and releases parameters. Plots show the relationship for (A) the error in
 320 emissions and releases for 1970 in the Streets et al. (30) inventory; (B) the error in emissions and
 321 releases for 1980; (C) the error in emissions and releases for 1990; (D) the error in emissions and
 322 releases for 2000; (E) the error in emissions and releases for 2010; (F) the trend in anthropogenic NH
 323 emissions for 2005–2020; (G) the trend in anthropogenic NH releases for 2005–2020. Black lines show
 324 median responses and the shaded area shows the 90% confidence interval (5th to 95th percentile). The
 325 slope (normalized to the range of the x-axis parameter) is listed on the plot to illustrate the relative
 326 importance of a parameter.
 327
 328

329 Section S7. Description of GEOS-Chem simulations
 330

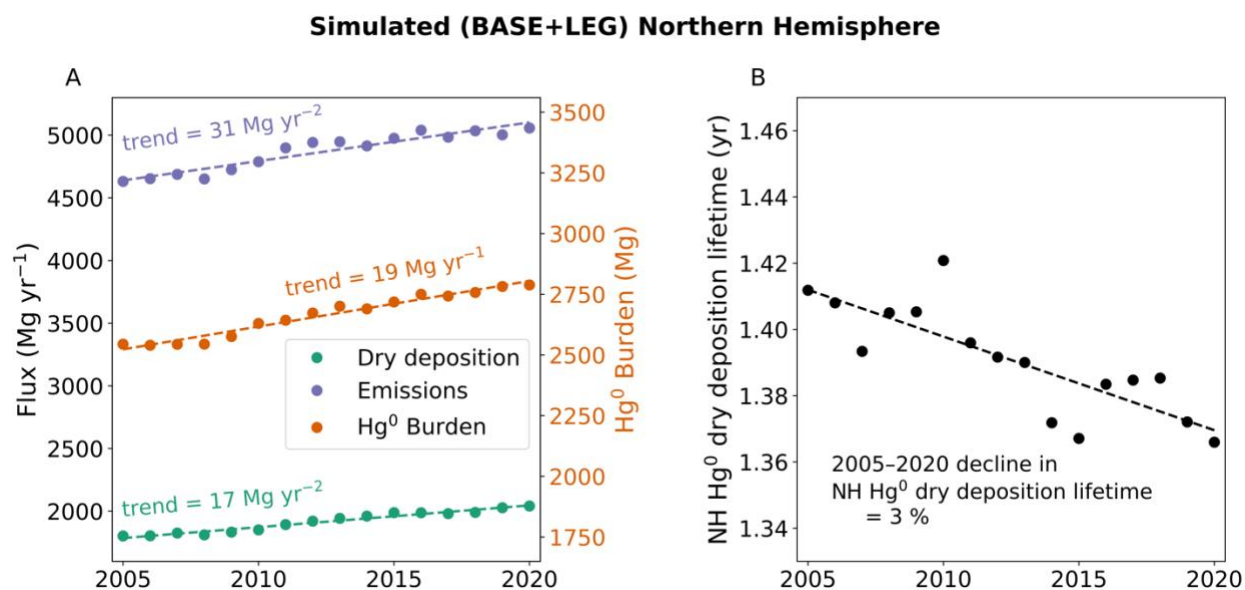


331
 332 **Figure S10.** The emission timeseries in GEOS-Chem simulations for 2005–2020: total emissions in the
 333 Northern Hemisphere (A), anthropogenic emissions in the Northern Hemisphere (B), total emissions in
 334 the Southern Hemisphere (C), and anthropogenic emissions in the Southern Hemisphere (D).
 335
 336

337 Section S8. Dry deposition trend in GEOS-Chem simulations

338 The Leaf Area Index (LAI) data used in GEOS-Chem comes from a reprocessed version of the Moderate
 339 Resolution Imaging Spectroradiometer (MODIS) satellite product (32), and includes the observed
 340 interannual variations in vegetation. Our GEOS-Chem simulations thus include the impact of (LAI)
 341 variations during 2005–2020 on the dry deposition of Hg^0 . The dry deposition scheme of GEOS-Chem
 342 and its response to changes in LAI have been thoroughly evaluated against observations by previous
 343 studies (33, 34). Here we evaluate the trends in the NH dry deposition of Hg^0 to investigate whether it is a
 344 major driver of the Hg^0 trends between 2005–2020.

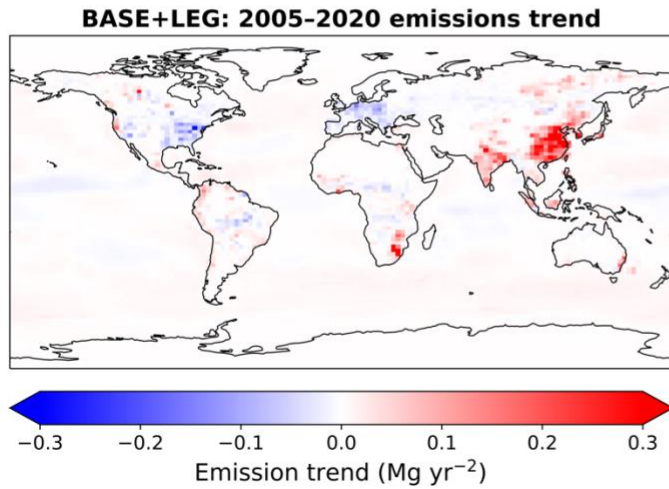
345
 346 Figure S11A shows the GEOS-Chem simulated fluxes of dry deposition over the BASE+LEG simulation.
 347 The dry deposition flux in the NH increases by 17 Mg yr^{-2} over the simulation, yet this is mainly due to the
 348 increasing emissions in the BASE+LEG scenario ($+31 \text{ Mg yr}^{-2}$ trend over simulation) increasing the
 349 amount of Hg^0 in the atmosphere. By dividing the NH Hg^0 burden by the dry deposition flux, we can
 350 calculate the dry deposition lifetime in the NH over the simulation (Fig. S11B). One observes a slight
 351 decline in the lifetime of Hg^0 dry deposition in the GEOS-Chem simulations over this time period, with a
 352 total decline in the lifetime of 3% between 2005 and 2020. Thus GEOS-Chem shows that the NH dry
 353 deposition of Hg^0 is indeed becoming faster over this time period, but not to the extent that it would
 354 reverse the emission driven changes in Hg^0 (Fig. 3C). Therefore, although it is important to further
 355 evaluate the impacts of changing vegetation on Hg cycling and its evolution in the future, during the
 356 2005–2020 time period the dry deposition lifetime trends have a small impact compared to the estimated
 357 changes in anthropogenic Hg emissions.
 358



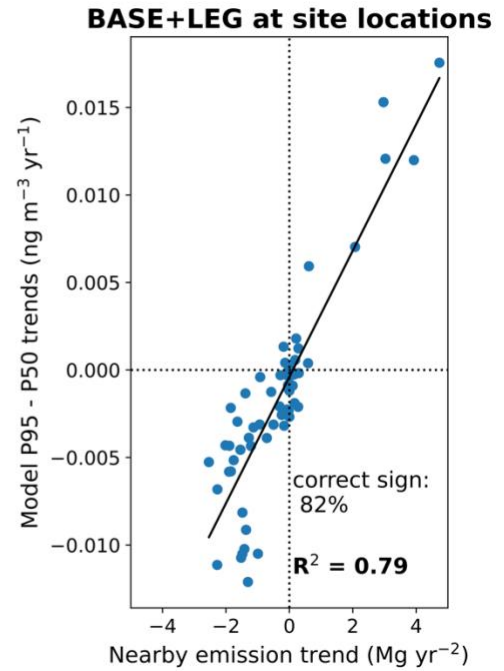
359 **Figure S11.** Impacts of changing vegetation on the dry deposition of Hg^0 in the NH. (A) Trends in the NH
 360 fluxes of dry deposition and total emissions in the BASE+LEG simulation (left y axis), along with changes
 361 in the NH Hg^0 burden (right y axis). Linear trend values are listed on the plot. (B) Trend in the Hg^0 NH dry
 362 deposition lifetime over the simulation, with the relative change between 2005 and 2020 listed on the plot.
 363
 364

365 Section S9. Additional quantile regression plots
 366

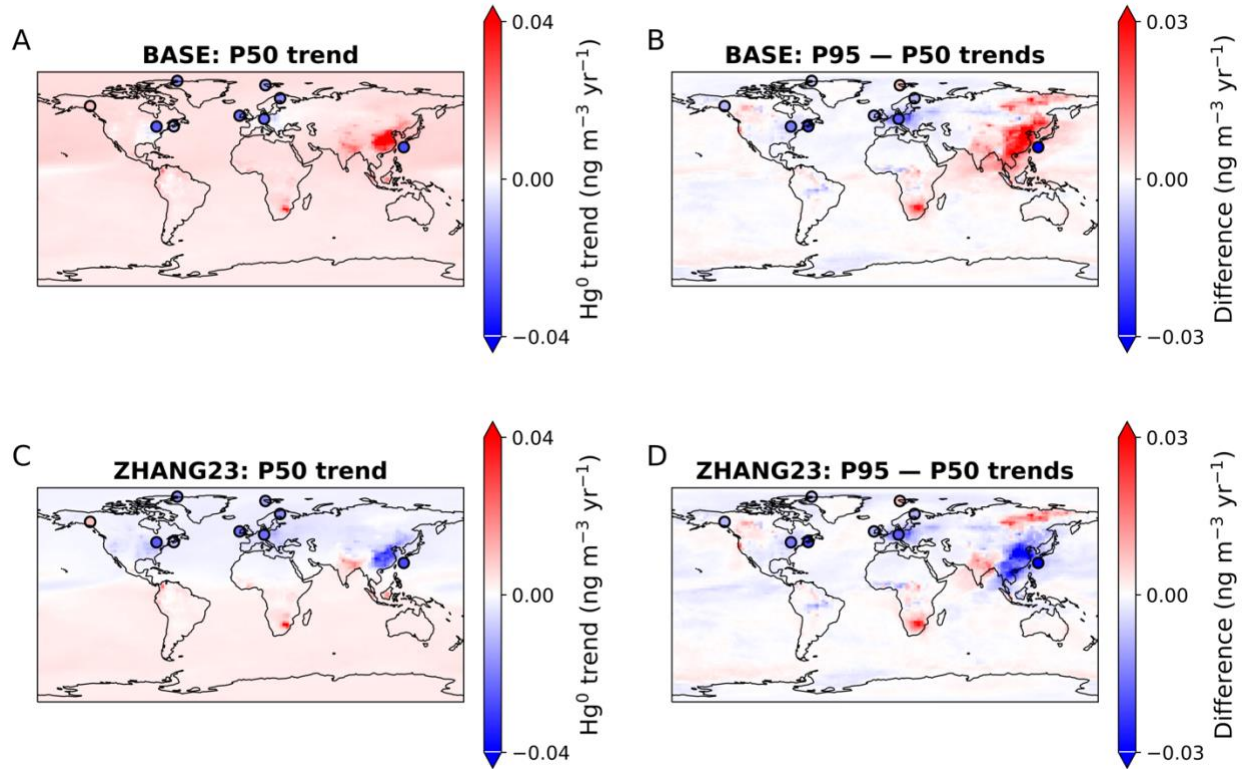
A



B



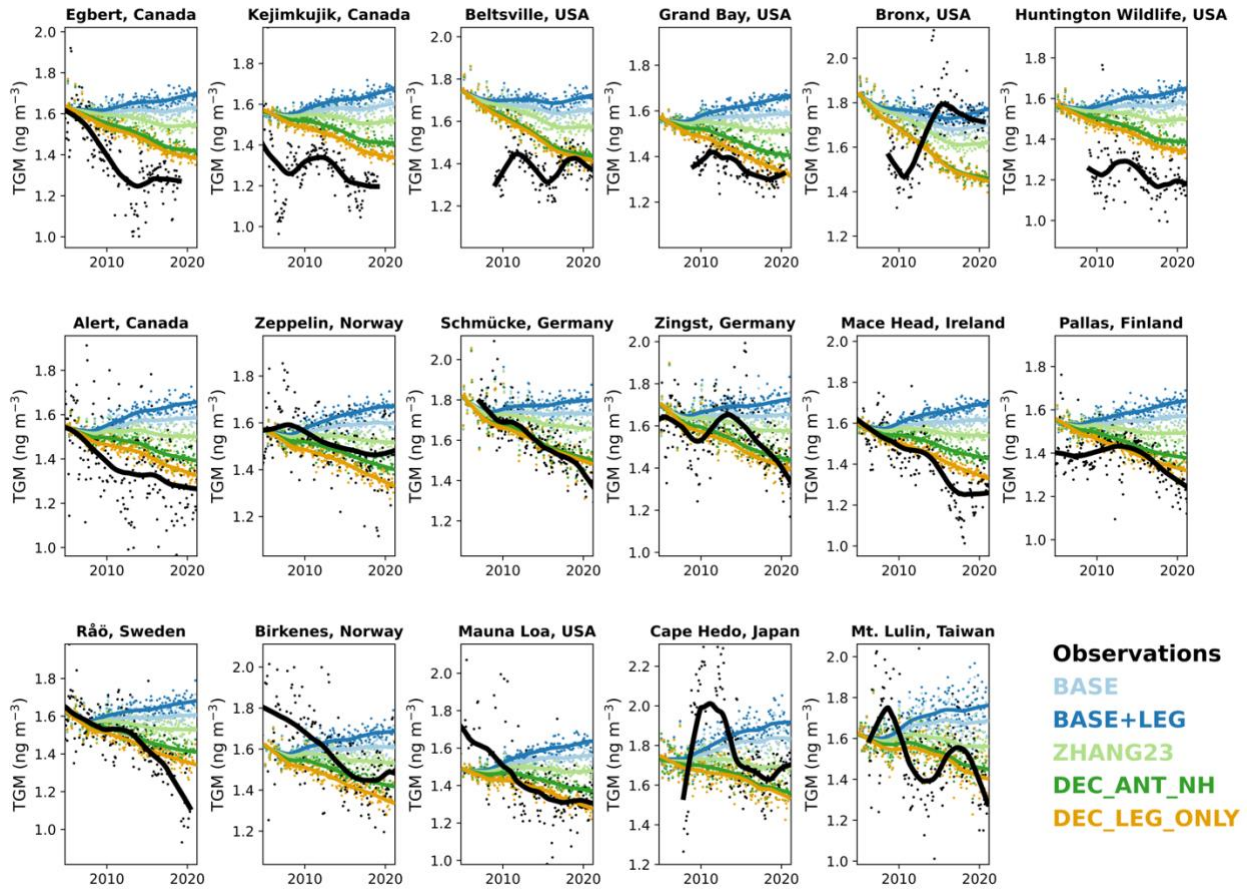
367
 368 **Figure S12.** (A) Map of the linear trend of Hg emissions in the BASE+LEG simulation between 2005 and
 369 2020. (B) Comparing the relationship between the BASE+LEG simulated nearby emission trend and the
 370 difference between the 95th percentile (P95) and median (P50) quantile regression Hg⁰ trends at grid
 371 boxes corresponding to site locations (see Fig. 4C for the full P95 – P50 trends map). The nearby
 372 emission trend is calculated by summing emissions trends within two grid boxes (~500 km) of the site
 373 location grid box.
 374



375
376
377
378
379
380

Figure S13. Trend in median (P50) daily deseasonalized simulated values in BASE (A) and ZHANG23 (C) for each model grid cell. Observed results are plotted in filled circles for 9 stations with more than 13 years of high frequency data. Differences between 95th percentile (P95) trend and median (P50) trend shown for BASE (B) and ZHANG23 (D) simulations and observations. The other simulations (BASE+LEG, DEC_ANT_NH, and DEC_LEG_ONLY) are shown in Fig. 4.

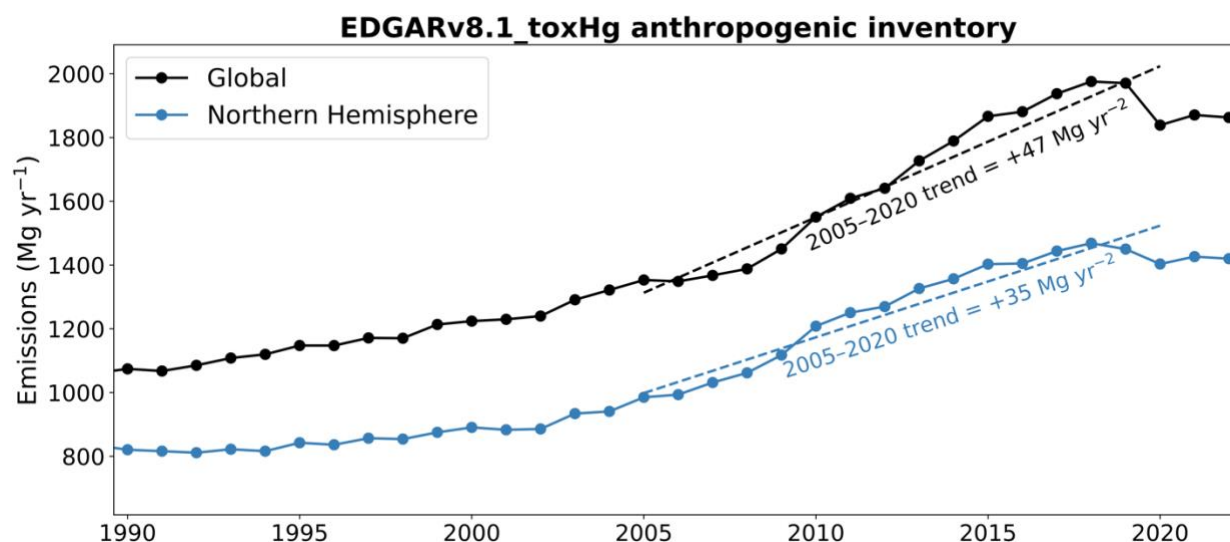
381 Section S10. Additional comparisons between observations and model simulations
 382



383
 384 **Figure S14.** Timeseries plots comparing model simulations (colors) and observations (black) at stations
 385 with more than 12 years of data during 2005–2020. Markers show deseasonalized monthly means and
 386 lines show the smoothed tendency of the time series calculated using LOWESS (locally weighted
 387 scatterplot smoothing) regression.
 388

389 **Section S11. EDGAR v8.1_toxHg emissions inventory**

390 A new anthropogenic emissions inventory has recently been released for 1970–2022, the EDGAR
 391 v8.1_toxHg inventory (35). Compared to the previous iteration of this inventory (EDGAR v4.tox2) (29),
 392 the v8.1 inventory includes updated spatial proxies and emissions factors and is extended to 2020. The
 393 released speciation maps (Hg^0 , Hg^{2+} , Hg^{P}) from the inventory were still in draft form at the time of this
 394 manuscript, so we did not run GEOS-Chem simulations with v8.1_toxHg, though this will be upcoming in
 395 the MCHgMAP project (36). The total Hg emissions maps have been released in definitive form at this
 396 time, so we have analyzed the trends in the total emissions (Fig. S15). The NH trend between 2005 and
 397 2020 is 35 Mg yr^{-2} , very similar to the Streets et al. (28) 2005–2015 trend (34 Mg yr^{-2}). Therefore, our
 398 modelling results using the Streets et al. (28) emissions trends are likely applicable to the new EDGAR
 399 v8.1_toxHg inventory as well. Increasing global and NH emissions are a common feature in both Streets
 400 et al. (28) and EDGAR v8.1_toxHg inventories, in contrast to the observed decline in Hg^0 concentrations.
 401



402
 403 **Figure S15.** Anthropogenic emissions trend from the EDGARv8.1_tox anthropogenic inventory, with
 404 linear trends calculated and plotted for the 2005–2020 period.
 405

406 **Supplementary References**

- 407 1. M. Iturbide, *et al.*, An update of IPCC climate reference regions for subcontinental analysis of
 408 climate model data: definition and aggregated datasets. *Earth Syst. Sci. Data* **12**, 2959–2970
 409 (2020).
- 410 2. D. A. Gay, *et al.*, The Atmospheric Mercury Network: measurement and initial examination of an
 411 ongoing atmospheric mercury record across North America. *Atmos. Chem. Phys.* **13**, 11339–11349
 412 (2013).
- 413 3. F. Carbone, *et al.*, Sea surface temperature variation linked to elemental mercury concentrations
 414 measured on Mauna Loa. *Geophys. Res. Lett.* **43**, 7751–7757 (2016).
- 415 4. F. Sprovieri, *et al.*, Atmospheric mercury concentrations observed at ground-based monitoring sites
 416 globally distributed in the framework of the GMOS network. *Atmos. Chem. Phys.* **16**, 11915–11935
 417 (2016).
- 418 5. A. Cole, *et al.*, A Survey of Mercury in Air and Precipitation across Canada: Patterns and Trends.
 419 *Atmosphere* **5**, 635–668 (2014).
- 420 6. V. L. St. Louis, *et al.*, Atmospheric Concentrations and Wet/Dry Loadings of Mercury at the Remote
 421 Experimental Lakes Area, Northwestern Ontario, Canada. *Environ. Sci. Technol.* **53**, 8017–8026
 422 (2019).

- 423 7. K. Tørseth, *et al.*, Introduction to the European Monitoring and Evaluation Programme (EMEP) and
 424 observed atmospheric composition change during 1972–2009. *Atmos. Chem. Phys.* **12**, 5447–5481
 425 (2012).
- 426 8. L. S. P. Nguyen, G.-R. Sheu, D.-W. Lin, N.-H. Lin, Temporal changes in atmospheric mercury
 427 concentrations at a background mountain site downwind of the East Asia continent in 2006–2016.
 428 *Science of The Total Environment* **686**, 1049–1056 (2019).
- 429 9. K. Marumoto, *et al.*, Long-Term Observation of Atmospheric Speciated Mercury during 2007–2018
 430 at Cape Hedo, Okinawa, Japan. *Atmosphere* **10**, 362 (2019).
- 431 10. Y. Zhang, *et al.*, Observed decrease in atmospheric mercury explained by global decline in
 432 anthropogenic emissions. *Proc. Natl. Acad. Sci. U.S.A.* **113**, 526–531 (2016).
- 433 11. K.-L. Chang, *et al.*, Trend detection of atmospheric time series. *Elementa: Science of the*
 434 *Anthropocene* **9**, 00035 (2021).
- 435 12. S. N. Wood, Fast stable restricted maximum likelihood and marginal likelihood estimation of
 436 semiparametric generalized linear models. *Journal of the Royal Statistical Society (B)* **73**, 3–36
 437 (2011).
- 438 13. K.-L. Chang, M. G. Schultz, G. Koren, Selke, Niklas, Guidance note on best statistical practices for
 439 TOAR analyses. Available at: <https://doi.org/10.48550/arXiv.2304.14236>. (2023).
- 440 14. P. S. Weiss-Penzias, *et al.*, Trends in mercury wet deposition and mercury air concentrations across
 441 the U.S. and Canada. *Science of The Total Environment* **568**, 546–556 (2016).
- 442 15. M. S. Gustin, *et al.*, Measurement of Atmospheric Mercury: Current Limitations and Suggestions for
 443 Paths Forward. *Environ. Sci. Technol.* **58**, 12853–12864 (2024).
- 444 16. M. S. Gustin, *et al.*, Do We Understand What the Mercury Speciation Instruments Are Actually
 445 Measuring? Results of RAMIX. *Environ. Sci. Technol.* **47**, 7295–7306 (2013).
- 446 17. A. Steffen, *et al.*, A synthesis of atmospheric mercury depletion event chemistry in the atmosphere
 447 and snow. *Atmospheric Chemistry and Physics* **8**, 1445–1482 (2008).
- 448 18. K. MacSween, *et al.*, Updated trends for atmospheric mercury in the Arctic: 1995–2018. *Science of*
 449 *The Total Environment* **837**, 155802 (2022).
- 450 19. D. Custódio, *et al.*, Odds and ends of atmospheric mercury in Europe and over the North Atlantic
 451 Ocean: temporal trends of 25 years of measurements. *Atmos. Chem. Phys.* **22**, 3827–3840 (2022).
- 452 20. J. Gačnik, S. Lyman, S. M. Dunham-Cheatham, M. S. Gustin, Limitations and insights regarding
 453 atmospheric mercury sampling using gold. *Analytica Chimica Acta* **1319**, 342956 (2024).
- 454 21. N. E. Selin, A proposed global metric to aid mercury pollution policy. *Science* **360**, 607–609 (2018).
- 455 22. H. M. Amos, D. J. Jacob, D. G. Streets, E. M. Sunderland, Legacy impacts of all-time anthropogenic
 456 emissions on the global mercury cycle. *Global Biogeochem. Cycles* **27**, 410–421 (2013).
- 457 23. H. M. Amos, *et al.*, Global Biogeochemical Implications of Mercury Discharges from Rivers and
 458 Sediment Burial. *Environ. Sci. Technol.* **48**, 9514–9522 (2014).
- 459 24. M. D. McKay, R. J. Beckman, W. J. Conover, Comparison of Three Methods for Selecting Values of
 460 Input Variables in the Analysis of Output from a Computer Code. *Technometrics* **21**, 239–245
 461 (1979).
- 462 25. H. M. Horowitz, *et al.*, A new mechanism for atmospheric mercury redox chemistry: implications for
 463 the global mercury budget. *Atmos. Chem. Phys.* **17**, 6353–6371 (2017).
- 464 26. J. P. Parrella, *et al.*, Tropospheric bromine chemistry: implications for present and pre-industrial
 465 ozone and mercury. *Atmos. Chem. Phys.* **12**, 6723–6740 (2012).
- 466 27. Y. Zhang, *et al.*, An updated global mercury budget from a coupled atmosphere-land-ocean model:
 467 40% more re-emissions buffer the effect of primary emission reductions. *One Earth* **6**, 316–325
 468 (2023).
- 469 28. D. G. Streets, *et al.*, Global and regional trends in mercury emissions and concentrations, 2010–
 470 2015. *Atmospheric Environment* **201**, 417–427 (2019).
- 471 29. M. Muntean, *et al.*, Evaluating EDGARv4.tox2 speciated mercury emissions ex-post scenarios and
 472 their impacts on modelled global and regional wet deposition patterns. *Atmospheric Environment*
 473 **184**, 56–68 (2018).
- 474 30. D. G. Streets, *et al.*, Five hundred years of anthropogenic mercury: spatial and temporal release
 475 profiles. *Environ. Res. Lett.* **14**, 084004 (2019).
- 476 31. H. Angot, *et al.*, Global and Local Impacts of Delayed Mercury Mitigation Efforts. *Environ. Sci.*
 477 *Technol.* **52**, 12968–12977 (2018).

- 478 32. H. Yuan, Y. Dai, Z. Xiao, D. Ji, W. Shangguan, Reprocessing the MODIS Leaf Area Index products
479 for land surface and climate modelling. *Remote Sens. Environ.* **115**, 1171–1187 (2011).
- 480 33. A. Feinberg, T. Dlamini, M. Jiskra, V. Shah, N. E. Selin, Evaluating atmospheric mercury (Hg)
481 uptake by vegetation in a chemistry-transport model. *Environ. Sci.: Processes Impacts* **24**, 1303–
482 1318 (2022).
- 483 34. A. Feinberg, M. Jiskra, P. Borrelli, J. Biswakarma, N. E. Selin, Deforestation as an Anthropogenic
484 Driver of Mercury Pollution. *Environ. Sci. Technol.* **58**, 3246–3257 (2024).
- 485 35. M. Muntean, *et al.*, EDGAR v8.1 Global Mercury Emissions. European Commission, Joint Research
486 Centre (JRC) [Dataset] PID: <http://data.europa.eu/89h/83b507d7-5218-4dc5-95f9-0ec36f073204>.
487 Deposited 2024.
- 488 36. A. Dastoor, *et al.*, The Multi-Compartment Hg Modeling and Analysis Project (MCHgMAP): Mercury
489 modeling to support international environmental policy. *Geoscientific Model Development*
490 *Discussions* **2024**, 1–171 (2024).

491